JOURNAL OF GEOPHYSICAL RESEARCH, VOL. 95, NO. B6, PAGES 8617–8638, JUNE 10, 1990

Transmission of Seismic Waves Across Single Natural Fractures

LAURA J. PYRAK-NOLTE[1]

Department of Materials Science and Mineral Engineering and Lawrence Berkeley Laboratory Earth Sciences Division, University of California, Berkeley

LARRY R. MYER

Lawrence Berkeley Laboratory, Earth Sciences Division, University of California, Berkeley

NEVILLE G. W. COOK

Department of Materials Science and Mineral Engineering and Lawrence Berkeley Laboratory Earth Sciences Division, University of California, Berkeley

Fractures and other nonwelded contacts are important mechanical and hydrological features of rock masses. Their effects on seismic wave propagation can be modeled as a boundary condition in the seismic wave equation. Seismic stress is continuous across such a boundary, but seismic particle displacement and seismic particle velocity are not. The complete solutions for seismic wave reflection, conversion, and transmission across a displacement and velocity discontinuity between two half-spaces with different densities and elastic properties are derived for all angles of the incident wave. The ratio between the seismic stress across this boundary and the seismic particle displacement and velocity are described by a specific stiffness and a specific viscosity, respectively. A displacement discontinuity results in frequency-dependent reflection and transmission coefficients and a frequency-dependent group time delay. The velocity discontinuity results in frequency-independent coefficients and zero delay. Results of laboratory experiments on compressional and shear wave transmission across three different natural fractures in a quartz monzonite are described. Measurements were made at different effective stresses under dry and saturated conditions at room temperature. It is shown that the effect of these fractures on the spectral amplitudes for compressional and shear pulses transmitted across these fractures are described well by a displacement discontinuity for compressional pulses under dry and saturated conditions and by a combined displacement and velocity discontinuity for shear wave pulses under dry and saturated conditions. Values of specific stiffness and specific viscosity vary between fractures and increase with increasing effective stress, as does the static specific stiffness of these fractures. Changes in the spectral amplitudes of transmitted pulses are also analyzed in terms of attenuation using the seismic quality factor Q, which is found to be a function of frequency.

INTRODUCTION

Seismic waves propagated through fractured rock masses are known to be slowed and attenuated. These effects of fractures on wave propagation are seen for fractures at all scales from microcracks to crustal faults. Often, the effect of fractures on seismic wave velocities has been modeled by first developing expressions for the effective elastic moduli of the fractured rock mass and then relating these expressions to velocity through the elastic-dynamic equations. Most of these models are based on populations of many small cracks, with dimensions much smaller than seismic wavelengths. For example, *O'Connell and Budiansky* [1974] used the self-consistent approach for the calculation of effective moduli of cracked solids under static loading conditions and predicted velocities under partially saturated conditions and for variations in crack density. If there is a preferred orientation of cracks or fractures, the effective elastic moduli will be anisotropic, giving rise to velocities which vary with the direction of propagation [*Crampin*, 1981]. Seismic velocities for a rock mass containing parallel fractures of areal extent large in comparison with wavelength have been derived by *White* [1983]. He modeled a fracture as two planes of infinite extent separated by hertzian contacts and derived effective anisotropic moduli assuming static loading conditions.

Seismic velocities derived from models such as those described above do not depend upon the frequency of the propagating waves. However, for dissipative media this frequency independence violates the principle of causality [*White*, 1983], and experimental results showing velocity dispersion have been obtained for rocks of widely varying porosities under different degrees of saturation for frequencies from 1 Hz to 1 MHz [*Jones and Nur*, 1983; *Winkler*, 1983; *Spencer*, 1981]. A correlation between velocity dispersion in saturated rocks and viscous interaction between solid and fluid phases has been postulated by *Spencer* [1981] and *Winkler* [1985, 1986].

A common approach to describing wave propagation in dissipative media is to relate the stress and strain amplitudes by a complex material modulus [*White*, 1983]. For an isotropic material, two independent complex moduli are required. *Crampin* [1981] has followed the same approach for anisotropic media, increasing the number of complex moduli as

[1]Now at Department of Earth and Atmospheric Sciences, Purdue University, East Lafayette, Indiana.

Paper number 90JB00129.
0148-0227/90/90JB-00129$05.00

required by the degree of anisotropy; for example, for transversely isotropic media, five complex moduli are required. A result of this approach is that strain is out of phase with stress by an amount given by the ratio of the real to imaginary parts of the modulus. The inverse of this phase angle is commonly referred to as the quality factor Q and is related to the energy loss per cycle (wavelength) for a wave propagating through a dissipative rock mass.

It has often been assumed, with supporting laboratory data [e.g., *Johnston and Toksöz*, 1980], that attenuation is frequency independent, and many theoretical models have been developed on the basis of this assumption (*Kjartansson* [1979] presented a good summary) even though this assumption violates causality. More recent laboratory work [*Spencer*, 1981; *Winkler and Nur*, 1982; *Winkler*, 1985] has shown that Q, particularly for partially saturated and saturated porous rocks, is frequency dependent.

A number of physical mechanisms have been proposed to explain observed attenuation (*Johnston et al.* [1979] presented a good review). Principal among these mechanisms are frictional sliding in cracks, viscosity and fluid flow in cracks, and scattering. Assuming a model in which wavelengths were large in comparison to crack length, *Walsh* [1966] evaluated the energy dissipated by relative motion (sliding) between the two surfaces of a crack. *O'Connell and Budiansky* [1977] modeled rocks as a viscoelastic solid, incorporating effects of flow between cracks under saturated conditions in expressions for the complex moduli. *Mavko and Nur* [1979] further investigated fluid effects by calculation of energy dissipation by fluid movement in a partially saturated crack. Applying a scattering formulation, *Kuster and Toksöz* [1974] developed expressions for seismic velocities in rock under dry and saturated conditions. *Hudson* [1981] calculated the energy scattered by a crack and, assuming the crack length was small in comparison to the wavelength, developed expressions for attenuation in rock with given crack densities.

Models in which cracks are assumed to be small compared to wavelength or in which material characteristics are represented by effective moduli are not relevant to evaluating the effects of relatively large, sparsely spaced fractures. In particular, an effective modulus is neither correct nor appropriate when describing wave propagation through a fractured rock in which fracture spacing is of a magnitude comparable with, or larger than, the seismic wavelength. Single fractures of large planar extent cannot be represented by models for cracks small in length compared to wavelength. Yet, as discussed below, several studies have shown that single and sparsely spaced fractures can have significant effects on wave propagation.

From field and laboratory tests, *Morris et al.* [1964] noted that single fractures intersecting a borehole wall caused decreases in the amplitudes of acoustic borehole logs. *Yu and Telford* [1973] found that about 96% of the energy of incident waves in the 60-kHz range was reflected from a single fracture even after the fracture had been placed under load. In a laboratory test, in which an acoustic log was performed in a borehole in limestone containing a single fracture, *Kleinberg et al.* [1982] observed a shift in phase as well as decreases in amplitude of waves propagating across the fracture. *Medlin and Marsi* [1984] were able to detect the location of the advancing crack tip and fluid front and changes in fracture aperture in a laboratory hydrofracture experiment by noting changes in amplitude of acoustic waves propagating normal to the fracture. *King et al.* [1986] conducted a cross-hole experiment in which compressional and shear waves were propagated between four horizontal drill holes in the wall of a drift in a basalt rock mass. The basalt was pervasively fractured with vertical columnar joints predominating. The wavelength of the compressional waves was about 0.1 m while the spacing of the predominant jointing was about 0.2–0.5 m. The waves with propagation paths across the fractures between the basalt columns were of lower frequency, of smaller amplitude, and slower than those which propagated in a direction parallel to the columns.

The theory for seismic wave propagation across a displacement discontinuity is discussed in this paper. From a single set of assumptions this theory predicts changes in group travel times and reflection and transmission coefficients of seismic waves for a single fracture of any orientation relative to the direction of wave propagation. The basic premise of the model is that displacements of a seismic wave are discontinuous across a fracture while the average seismic stresses remain continuous. The ratio between the stress and the magnitude of the displacement discontinuity produced by it is defined as the specific stiffness of the fracture. The boundary condition of discontinuous displacements has previously been assumed by *Mindlin* [1960] in an analysis of compressional and shear wave coupling in a plate with elastically restrained edges. *Kendall and Tabor* [1971] also assumed discontinuous displacements in a solution for a compressional wave normally incident on an incomplete interface. The general solution of the elasto-dynamic equations for waves obliquely incident upon a single fracture for the displacement discontinuity boundary conditions has been given by *Schoenberg* [1980] and *Kitsunezaki* [1983]. *Schoenberg* [1983] extended the theory to the case of periodic displacement discontinuities in a stratified half-space. *Baik and Thompson* [1984] used distributed springs and masses to analyze ultrasonic scattering from imperfect interfaces. Experiments performed by *Myer et al.* [1985], using artificial fractures of calculable stiffness, provided validation of the seismic displacement discontinuity theory for single fractures and normally incident compression and shear waves. *Pyrak-Nolte and Cook* [1987] determined that an elastic interface wave exists along a nonwelded interface (displacement discontinuity).

In this paper, results are reported from a set of laboratory experiments in which compressional and shear pulses were propagated across single, natural fractures in crystalline rock at different normal stresses under dry and saturated conditions. Both velocities and spectral amplitudes were measured, and measured spectra were compared with those predicted by the seismic displacement discontinuity theory. Results are compared with those obtained from standard methods of attenuation analysis, and the applicability of the seismic displacement discontinuity theory to whole rock attenuation analysis is discussed.

Displacements Across a Fracture

Several studies have been made of the displacements produced by changes in normal and, sometimes, shear stresses across fractures. Many of these have used newly induced tensile fractures [*Goodman*, 1976; *Swan*, 1983],

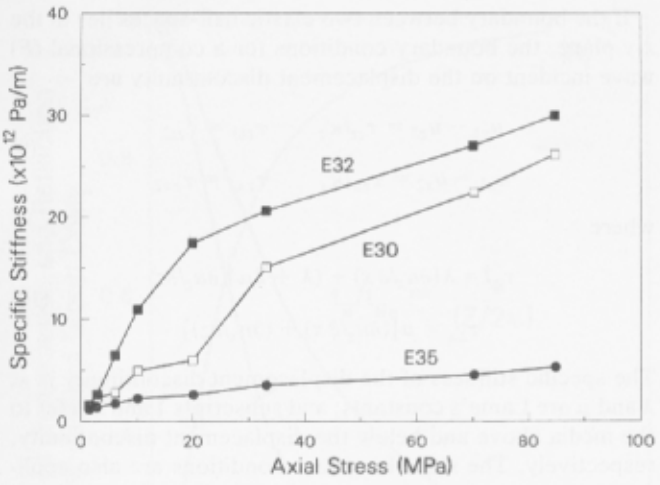

Fig. 1. Specific stiffnesses determined from displacement-stress data for fractured specimens E32, E30, and E35 as a function of stress.

while some have used natural fractures [*Bandis et al.*, 1983; *Raven and Gale*, 1985]. All these studies have shown that the normal displacement across a fracture is a strongly nonlinear function of the normal stress. *Goodman* [1976] has proposed a logarithmic relationship between displacements and stress, while *Bandis et al.* [1983] have proposed a hyperbolic relationship. Both Goodman and Bandis et al. have drawn attention to specific fracture stiffness, that is, the inverse of the slope of the tangent to the displacement-stress curve, as an important property of a fracture, which must also be a function of the applied stress.

Pyrak-Nolte et al. [1987*a*] have studied the relationship between the applied stress and the normal displacement across single natural fractures in laboratory specimens of quartz monzonite. Stress-displacement curves were measured for each of the fractures over a number of loading and unloading cycles up to a maximum uniaxial stress normal to the fracture of 85 MPa. The three fractures selected had very different displacement-stress characteristics, but the deformations were elastic [*Pyrak-Nolte et al.*, 1987*a*]. Smooth curves were fitted to the displacement-stress data, and the specific stiffness was found from the inverse of the slope of the tangents to these curves (Figure 1). These curves show that the specific stiffness of the fracture increases in a nonlinear fashion with increasing stress. It is seen that the fracture in sample E32 was the "stiffest," while that in E30 was of intermediate stiffness and the fracture in E35 was the most compliant.

For many fractures it seems likely that the thickness of the fracture, that is, the mean aperture between the two surfaces, will be less than the mean size of the asperities which will be less than the mean separation between asperities. All of these quantities are probably very much less than the spacing between fractures. For seismic wavelengths much greater than the mean separation between asperities but less than the fracture spacing, we propose that a fracture can be modeled as a displacement discontinuity, that is, as a boundary across which the seismic stress is continuous but the displacements are not. At any given stress across a fracture with rough surfaces in imperfect contact, there exists a particular geometry of asperities of contact and adjacent voids. An increment in stress produces elastic deformations of the asperities and voids that result in an increment of the displacement across the fracture, the ratio of these two quantities being the specific stiffness. This definition is considered valid for both static and dynamic loading conditions. It will be shown that an increment in stress produces an incremental displacement between any two planes parallel to the plane of the fracture and on each side of the fracture plane that is the same regardless of the separation between these planes. In other words, there exists a discontinuity in displacement across a fracture. Clearly, for static equilibrium the mean stress on each of any two planes parallel to the fracture plane is the same as the mean stress across the asperities in the fracture plane; that is, the mean stress across a fracture is continuous.

Consider two half-spaces bounded by rough surfaces that are in contact with one another over the x-y plane at $z = 0$. Let these half-spaces be subject to a uniform normal stress σ_z at values of $|z|$ that are large compared with the wavelengths of the composite surface roughness. The strains will be

$$\varepsilon_z = \partial w/\partial z \tag{1}$$

where w is the displacement in the z direction. Because the half-spaces are subject to uniaxial strain,

$$\int_{-\infty}^{+\infty}\int \frac{\partial u}{\partial x}\,dx\,dy = 0 = \int_{-\infty}^{+\infty}\int \frac{\partial v}{\partial y}\,dx\,dy \tag{2}$$

where u and v are displacements in the x and y directions. On planes where $|z|$ is comparable with the roughness of the surfaces, $\sigma_z(x, y)$ is a function of x and y, but for equilibrium,

$$\int_{-\infty}^{+\infty}\int \sigma_z(\text{const})\,dx\,dy = \int_{-\infty}^{+\infty}\int \sigma_z(x, y)\,dx\,dy = C(\sigma_z) \tag{3}$$

Using the elastic stress strain relations with λ and μ, Lame's constants, in (3) yields

$$\int_{-\infty}^{+\infty}\int \sigma_z(x, y)\,dx\,dy$$

$$= \int_{-\infty}^{+\infty}\int \left[(\lambda + 2\mu)\frac{\partial w}{\partial z} + \lambda\left(\frac{\partial u}{\partial x} + \frac{\partial v}{\partial y}\right)\right] dx\,dy = C(\sigma_z) \tag{4}$$

Since there can be no net displacements in the x or y directions, (4) becomes

$$\frac{\partial}{\partial z}\int_{-\infty}^{+\infty}\int w\,dx\,dy = \frac{C(\sigma_z)}{(\lambda + 2\mu)} \tag{5}$$

so that

$$\int_{-\infty}^{+\infty}\int w\,dx\,dy = \frac{C(\sigma_z)z}{(\lambda + 2\mu)} + G(\sigma_z) \tag{6}$$

Each of the terms in (6) is a function of the applied stress and represents a volumetric displacement of a plane $|z|$ = constant. These volumetric displacements can be changed to average linear displacements by dividing each term by the area of the plane, so that for each half-space

$$\left(\int_{-\infty}^{+\infty}\int w\,dx\,dy\right)\Bigg/\left(\int_{-\infty}^{+\infty}\int dx\,dy\right)$$

$$= \left\{\frac{C(\sigma_z)z}{(\lambda + 2\mu)} + G(\sigma_z)\right\}\Bigg/\left(\int_{-\infty}^{+\infty}\int dx\,dy\right) \tag{7}$$

Letting subscript 1 refer to the upper half-space, (7) can be written as

$$\langle w_1\rangle = z\,\frac{\langle C(\sigma_z)\rangle}{(\lambda + 2\mu)} + \langle G_1(\sigma_z)\rangle \tag{8a}$$

where the angle brackets indicate the average value over the area of the any plane z = constant. A similar expression can be written for the lower half-space.

Clearly the factor $\langle C(\sigma_z)\rangle/(\lambda + 2\mu)$ in the first term on the right-hand side of (8*a*) corresponds to the uniform strain ε_z that is present on planes far from $z = 0$. When the two surfaces are smooth, or in perfect contact, it represents the total strain on these planes. The second term on the right-hand side of (8*a*), $\langle G_1(\sigma_z)\rangle$, and a corresponding term, $\langle G_2(\sigma_z)\rangle$, for the lower half-space represent the displacements that arise because the rough surfaces are in imperfect contact. The difference between these two terms, $\langle G_1(\sigma_z)\rangle - \langle G_2(\sigma_z)\rangle = D(\sigma_z)$, constitutes the additional displacements, or the displacement discontinuity that occurs between any two planes $\pm z$.

As noted above, specific stiffness is defined as the ratio of the applied stress to average displacement it produces. In general, specific stiffness is a function of the stress across the fracture and is thus given by

$$\kappa = \frac{\partial\sigma_z}{\partial D(\sigma_z)} \tag{8b}$$

Seismic Theory of a Displacement Discontinuity

To theoretically model the effect of a fracture on the propagation of plane seismic waves, the fracture is represented as a displacement discontinuity at the boundary between two elastic half-spaces. It is assumed that the stress across the displacement discontinuity is continuous. The magnitude of the discontinuity in displacement is inversely proportional to the specific stiffness of the fracture.

If the boundary between two elastic half-spaces lies in the x-y plane, the boundary conditions for a compressional (P) wave incident on the displacement discontinuity are

$$\begin{aligned} u_{z1} - u_{z2} &= \tau_{zz}/\kappa_z \qquad \tau_{zz1} = \tau_{zz2} \\ u_{x1} - u_{x2} &= \tau_{zx}/\kappa_x \qquad \tau_{zx1} = \tau_{zx2} \end{aligned} \tag{9}$$

where

$$\begin{aligned} \tau_{zz} &= \lambda(\partial u_x/\partial x) + (\lambda + 2\mu)(\partial u_z/\partial z) \\ \tau_{zx} &= \mu[(\partial u_z/\partial x) + (\partial u_x/\partial z)] \end{aligned} \tag{10}$$

The specific stiffness of the displacement discontinuity is κ; λ and μ are Lame's constants; and subscripts 1 and 2 refer to the media above and below the displacement discontinuity, respectively. The same boundary conditions are also applicable to a plane shear wave polarized in the x-z plane (S_v wave).

For an incident shear wave with polarization in the x-y plane (S_h wave) the boundary conditions are

$$u_{y1} - u_{y2} = \tau_{zy}/\kappa_y \qquad \tau_{zy1} = \tau_{zy2} \tag{11}$$

where

$$\tau_{zy} = \mu(\partial u_y/\partial z) \tag{12}$$

For an incident P wave the components of displacement normal and parallel to the x-y plane satisfy the equations

$$\begin{aligned} \frac{\partial^2 u_x}{\partial t^2} &= \alpha^2\left(\frac{\partial^2}{\partial x^2} + \frac{\partial^2}{\partial z^2}\right)u_x \\ \frac{\partial^2 u_z}{\partial t^2} &= \alpha^2\left(\frac{\partial^2}{\partial x^2} + \frac{\partial^2}{\partial z^2}\right)u_z \end{aligned} \tag{13}$$

where α is the velocity of propagation for compressional plane waves. Similarly, for a S_v wave the displacements satisfy the equations

$$\begin{aligned} \frac{\partial^2 u_x}{\partial t^2} &= \beta^2\left(\frac{\partial^2}{\partial x^2} + \frac{\partial^2}{\partial z^2}\right)u_x \\ \frac{\partial^2 u_z}{\partial t^2} &= \beta^2\left(\frac{\partial^2}{\partial x^2} + \frac{\partial^2}{\partial z^2}\right)u_z \end{aligned} \tag{14}$$

where β is the velocity of propagation for shear plane waves. For a S_h wave the displacement u_y satisfies the equation

$$\frac{\partial^2 u_y}{\partial t^2} = \beta^2\,\frac{\partial^2 u_y}{dy^2} \tag{15}$$

The general solution for arbitrary angles of incidence and materials of different seismic impedance above and below the displacement discontinuity is given in the Appendix.

For waves normal to the displacement discontinuity with the same material properties in both half-spaces, the reflection and transmission coefficients $R(\omega)$ and $T(\omega)$ for incident P, S_v, and S_h waves are

$$\begin{aligned} R_p(\omega) &= i\omega/[-i\omega + 2(\kappa_z/Z_p)] \\ T_p(\omega) &= 2(\kappa_z/Z_p)/[-i\omega + 2(\kappa_z/Z_p)] \\ R_{sv}(\omega) &= -i\omega/[-i\omega + 2(\kappa_x/Z_s)] \end{aligned} \tag{16a}$$

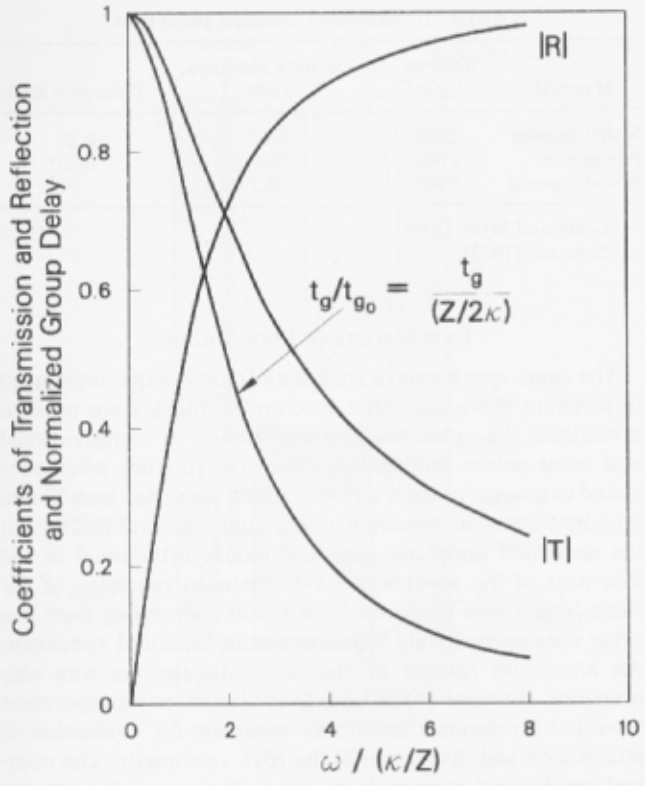

Fig. 2. Magnitudes of the reflection and transmission coefficients and normalized group delay for a seismic wave normally incident upon a displacement discontinuity as a function of normalized frequency.

$$T_{sv}(\omega) = 2(\kappa_x/Z_s)/[-i\omega + 2(\kappa_x/Z_s)]$$

$$R_{sh}(\omega) = -i\omega/[-i\omega + 2(\kappa_y/Z_s)]$$

$$T_{sv}(\omega) = 2(\kappa_y/Z_s)/[-i\omega + 2(\kappa_y/Z_s)]$$

where Z is the seismic impedance (Z = density × phase velocity). The group time delay across the displacement discontinuity can be found from the derivative of the phase with respect to frequency, that is, $t_{gr} = d\theta_T/d\omega$ where θ_T is the phase of the transmitted wave. For the transmitted wave the group delay is [*Pyrak-Nolte et al.*, 1987*b*]

$$t_{gr} = 2(\kappa/Z)/[4(\kappa/Z)^2 + \omega^2] \qquad (16b)$$

which is the same as that for the reflected wave.

Equations (16*a*) and (16*b*) are illustrated graphically in Figure 2 using dimensionless variables. The magnitudes of the reflected and transmitted waves are a function of frequency, as well as a function of the ratio of the specific stiffness of the displacement discontinuity to the seismic impedance of the material on either side of it. The theory predicts that a fracture should behave as a low-pass filter with a cutoff frequency which is determined by the ratio of specific stiffness of the displacement discontinuity to the seismic impedance of the half-spaces. Also, in this theory, energy is conserved at a displacement discontinuity, which can be shown by summing the squares of any pair of reflection and transmission coefficients, so that $|R(\omega)|^2 + |T(\omega)|^2 = 1$. As shown in Figure 2, the absolute value of the transmission coefficient, $|T|$, is a maximum at zero frequency while that of the reflection coefficient, $|R|$, is zero at zero frequency. The group time delay is a maximum at zero frequency and decreases with increasing frequency. As stiffness tends to infinity, the displacement discontinuity becomes equivalent to a welded interface, i.e., all the energy is transmitted. If the stiffness tends to zero, the displacement discontinuity reverts to the case of a free surface, and all the energy is reflected.

The presence of a liquid under saturated conditions in a joint or fracture will increase the specific stiffness of the displacement discontinuity for compressional waves and possibly for shear waves. The liquid may also introduce viscous coupling between the two surfaces of the fracture. *Schoenberg* [1980] derived a solution for an elastic wave propagated across a viscous interface, neglecting the stiffness of the interface. *Pyrak-Nolte* [1988] combined the effects of specific stiffness and specific viscosity on wave propagation across a fracture to yield discontinuities in both displacement and velocity while the stress across the discontinuity remained constant.

For an incident P wave or S_v wave the boundary conditions for the combined displacement and velocity discontinuities are

$$u_{z1} - u_{z2} = \tau_{zz}/\kappa_z \qquad \tau_{zz1} = \tau_{zz2}$$

$$\kappa_x(u_{x1} - u_{x2}) + \eta\left(\frac{\partial u_{x1}}{\partial t} - \frac{\partial u_{x2}}{\partial t}\right) = \tau_{zx} \qquad \tau_{zx1} = \tau_{zx2} \qquad (17)$$

where

$$\tau_{zz} = \lambda\{\partial u_x/\partial x\} + (\lambda + 2\mu)\{\partial u_z/\partial z\}$$

$$\tau_{zx} = \mu\{\partial u_z/\partial x + \partial u_x/\partial z\} \qquad (18)$$

and η is the specific viscosity, that is, the ratio between the stress across a fracture and the discontinuity in velocity that this produces. The units of η are viscosity per length. For an incident S_h wave the boundary conditions are

$$\kappa_y(u_{y1} - u_{y2}) + \eta\left(\frac{\partial u_{y1}}{\partial t} - \frac{\partial u_{y2}}{\partial t}\right) = \tau_{zy}$$

$$\tau_{zy1} = \tau_{zy2} \qquad (19)$$

where

$$\tau_{zy} = \mu\ \partial u_y/\partial z \qquad (20)$$

The complete solution in matrix form is given in the Appendix. For waves normal to the interface where the material properties in the two half-spaces are equal, the reflection and transmission coefficients $R(\omega)$ and $T(\omega)$ for incident P, S_v, and S_h waves are

$$R_P(\omega) = i\omega/(2\kappa_z/Z_p - i\omega)$$

$$T_P(\omega) = 2\kappa_z/Z_p/(2\kappa_z/Z_p - i\omega)$$

$$R_{sv}(\omega) = -i\omega Z_s/[2\kappa_x - i\omega(2\eta + Z_s)]$$

$$T_{sv}(\omega) = 2(\kappa_x - i\omega\eta)/[2\kappa_x - i\omega(2\eta + Z_s)] \qquad (21)$$

$$R_{sh}(\omega) = -i\omega Z_s/[2\kappa_y - i\omega(2\eta + Z_s)]$$

$$T_{sh}(\omega) = 2(\kappa_y - i\omega\eta)/[2\kappa_y - i\omega(2\eta + Z_s)]$$

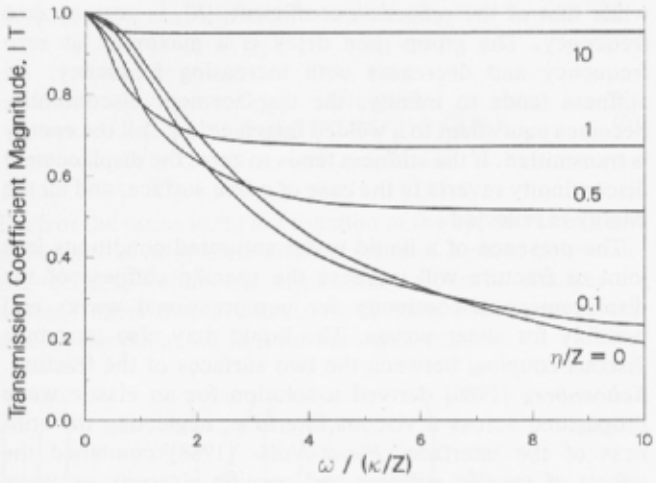

Fig. 3. Magnitudes of the transmission coefficient for a shear wave normally incident upon a combined displacement and velocity discontinuity as a function of normalized frequency for a range of normalized specific viscosities.

In the limit, when either κ or η tend to infinity, the solution reverts to that of a welded interface, and when both κ and η go to zero, it reverts to that of a free surface. Figure 3 shows the magnitude of the transmission coefficient $|T|$ for S waves as a function of the dimensionless variable $\omega/(\kappa/Z)$ for a range of values of η/Z. For $\eta/Z = 0$ (specific viscosity of zero) the curve is identical to that obtained using (16a) and shown in Figure 2. Compared with the solution for a dry interface, the effect of finite values of specific viscosity is to reduce the energy transmitted at low frequencies and increase the energy transmitted at high frequencies. Also, $|T|$ becomes independent of frequency when the specific viscosity term dominates the solution.

It should be noted that for a viscous interface, $|R(\omega)|^2 + |T(\omega)|^2 \neq 1$, because energy is dissipated owing to the presence of the fluid in the joint. The presence of the fluid enhances transmission by improving the coupling between the surfaces but at the same time reduces the amplitudes of the transmitted and reflected pulses by viscous losses.

TABLE 1. Assumed Material Properties

Material	Density, kg/m^3	Young's Modulus, GPa	Poisson's Ratio
Stripa granite	2650	60.*	0.25
Aluminum	2700†	68.†	0.33†
Wood's metal	9400	9.7	...

*_Cook and Myer_ [1981].
†_Eshbach_ [1952].

EXPERIMENTAL PROCEDURE

The same specimens of rock with fractures that were used to measure the quasi-static fracture stiffness were used to investigate the velocities and attenuation of compressional and shear pulses propagated across the fracture when subjected to a range of axial stresses. Each specimen was 77 mm long by 52 mm in diameter with a single natural fracture at the specimen midplane, oriented nearly orthogonal to the long axis of the specimens. A companion specimen of the same length was prepared from intact rock taken from the same core immediately adjacent to the fractured specimen. An aluminum sample of the same dimensions was also prepared. Because of the high Q of aluminum this specimen provided a reference amplitude spectrum for evaluation of attenuation and dispersion in the rock specimens. The nominal mechanical properties of intact Stripa granite and the aluminum specimen are given in Table 1.

Measurements were carried out using the test systems illustrated in Figure 4. The specimens were compressed between steel transducers containing piezoelectric elements in a servocontrolled test machine (Figure 4). The ends of the specimens and those of the transducers were ground flat and parallel to within 10 μm to ensure both uniform axial loading and good contact between the specimen and the transducers. Chemical cleaning of the surfaces and the insertion of a thin lead foil, 25 μm thick, between the ends of the specimens and the transducers were found to improve the magnitude and reproducibility of the seismic coupling between these parts.

The seismic transducers were designed to yield strong and reproducible signals. One transducer contains the compres-

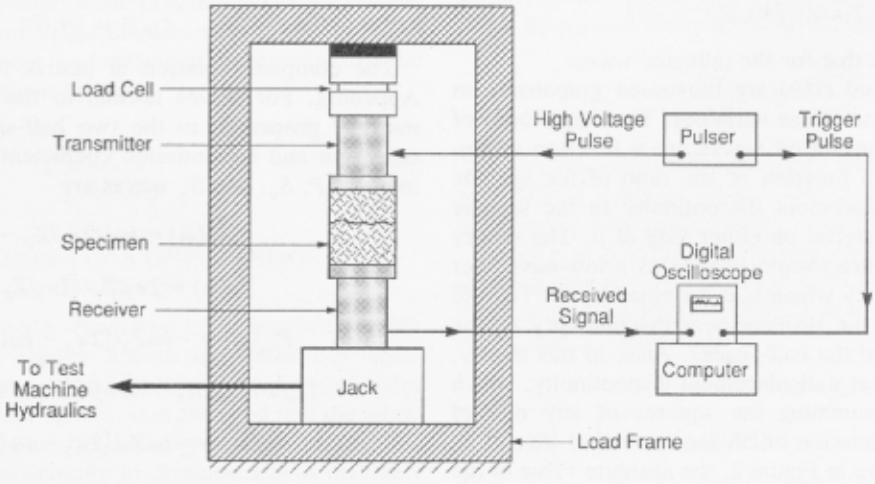

Fig. 4. Schematic illustration of test system for seismic measurements on fractured and intact specimens.

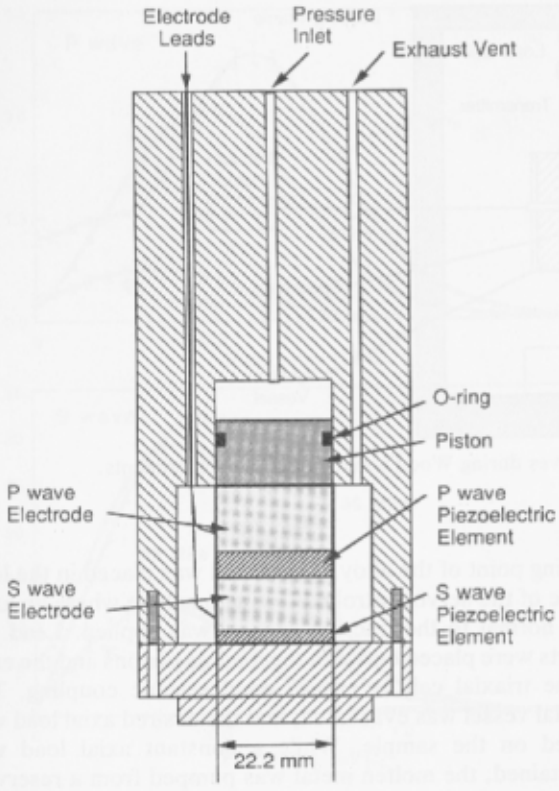

Fig. 5. Cross section of transducer showing arrangement of electrodes and piezoelectric elements.

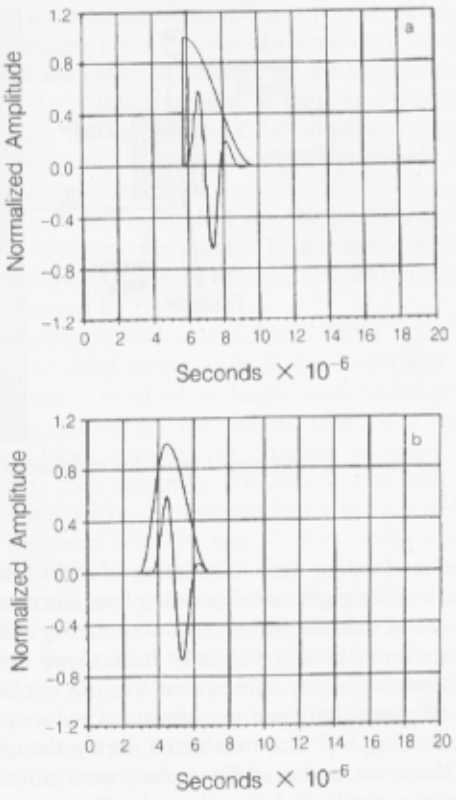

Fig. 6. Examples of tapers applied to seismic pulses and resulting waveforms obtained from fractured specimen E35, dry condition, 85 MPa: (*a*) half cosine taper with 4.0-μs window for *P* waves; (*b*) taper for *S* waves consisting of half cosine 1.5-μs opening and half cosine 2.5-μs closing. Pulses were normalized to maximum amplitude prior to tapering.

sional and shear crystals for transmission, and the other those for reception of the seismic pulses. The end of each transducer in contact with the rock is closed by a thick hardened steel plug with surfaces ground parallel to one another. The piezoelectric crystals and their electrodes are stacked sequentially behind each end closure (Figure 5). Pressing against the last electrode is a piston with an O ring seal. The space behind this piston is held at a constant nitrogen pressure of 27.5 MPa while the portion of the cylinder in front of the piston containing the crystal electrode assembly is vented. A nitrogen pressure in excess of 24 MPa ensures good, reproducible seismic coupling between the crystals and the end closure in contact with rock specimen.

The natural frequency of each crystal was 1 MHz, and the transmission crystals were pulsed with a 500-V spike of 0.3 μs duration at a repetition rate of 100 Hz (Velonex high-power pulse generator, model 350). The signals detected by the receiver crystals were terminated with a 50-ohm impedance and dc coupled to a Tektronics (model 7704A) digital oscilloscope. The oscilloscope was triggered by a pulse from the high-voltage pulser through a calibrated variable time delay on the oscilloscope so that the arrival time of each pulse cold be read to 0.01 μs. Group arrival times were measured for both compressional and shear waves. The system delay time was determined by linear regression of arrival times using data from aluminum specimens of different lengths together with lead foil inserts on each end. The system delay for compressional waves was 16.52 $\pm$ 0.03 μs and for shear waves was 22.96 $\pm$ 0.13 μs.

The oscilloscope was used to digitize and store a portion of each seismic pulse with a duration of 20 μs. These pulses were digitized (Tektronics P7001 digitizer) at a rate of 25.6 points/μs, and three such digitized pulses were stacked to produce a good signal to noise ratio. The oscilloscope was connected to a PDP 11/44 computer where each record was stored on floppy disc.

To examine the spectral content of the pulses, the received seismic signals were tapered to isolate the initial arrival pulse of the *P* wave and the *S* wave from subsequent reflections. A half cosine taper with a 4.0-μs window (Figure 6*a*) was applied to the *P* wave signals, while a taper consisting of a half wave cosine taper 1.5-μs opening and a one-half cosine taper 2.5-μs closing (Figure 6*b*) was applied to the *S* wave signals. The first criterion in selecting the shape and duration for the taper was to ensure that it not alter significantly the spectrum of the source pulse. The second criterion was that the taper should isolate the initial *P* and *S* pulses from the reflections and yet preserve much of the low-frequency content of the signal without too much distortion in the high-frequency range. Experiments with a variety of tapers showed that spectra of the first pulse obtained with tapers chosen according to these criteria did not depend critically on the precise shape and duration of the taper. The same tapers were applied to all of the collected signals. Amplitude spectra were calculated by performing a fast Fourier transform (FFT) on the tapered waveforms. Seismic measurements were made on each type of specimen (intact, fractured, aluminum) over a range of uniaxial stresses from 1.4 MPa to 85 MPa. Measurements were made

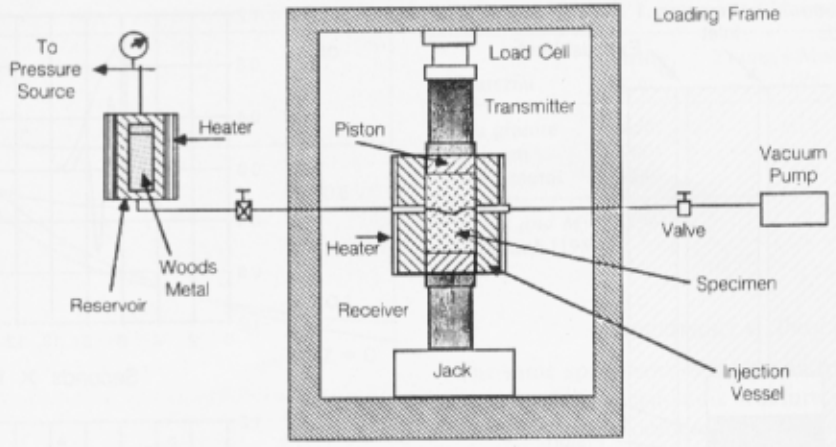

Fig. 7. Experimental setup for measurement of P and S waves during Wood's metal injection experiments.

for a complete loading cycle consisting of eight load increments followed by eight corresponding load decrements.

Waveforms of seismic pulses measured during initial loading were observed to differ slightly from those during unloading. However, upon subsequent loading cycles, there was little difference between waveforms of pulses collected during the loading and those collected during the unloading portion of the cycle, and in addition, they were indistinguishable from those obtained during the unloading portion of the initial loading cycle. Therefore the results presented in the paper are based on the waveforms of pulses collected during the unloading portion of the initial loading cycles.

Data were collected under three different experimental conditions as described below.

1. For tests at oven dry conditions, intact and fractured samples were oven-dried at about 100°C for many hours prior to testing.

2. For saturated conditions the samples were vacuum-saturated prior to testing. When the fractured sample was placed in the test frame, a rubber membrane was placed around it, and the fracture was vacuum-saturated. The water pressure was then maintained at a value which did not exceed about 0.3 MPa.

3. One fractured specimen was used in experiments that involved filling the fracture voids with molten metal, collecting seismic data, and then allowing the metal to solidify and collecting seismic data again. The purpose of this experiment was to evaluate the extent to which the attenuation caused by a fracture would be changed by filling the fracture voids with a material that has approximately the same seismic impedance as the intact rock. The metal used to fill the fracture voids is one of a family of bismuth-lead-tin alloys of which Wood's metal is the most commonly recognized. In the liquid phase, these are nonwetting with an effective surface tension about 400 MN/m [*Yadav et al.*, 1984]. The particular alloy used (Cerrosafe®) has a nominal composition of 0.42 Bi, 0.38 Pb, 0.11 Sn, and 0.08 Cd and a melting point of 160°–190°F. On the basis of Young's modulus of 9.7 GPa and a density of 9400 kg/m^3 the compressional seismic impedance of this alloy in the solid state is about 9.5×10^6 Pa/ms, compared with about 1.2×10^7 Pa/ms for the rock.

A schematic drawing of the metal injection apparatus is shown in Figure 7. The sample was held in a triaxial test vessel which was maintained at a temperature just above the melting point of the alloy. The vessel was placed in the load frame of the servocontrolled testing machine where an axial load normal to the fracture surface was applied. Lead foil inserts were placed between the loading pistons and the ends of the triaxial cell to ensure good seismic coupling. The triaxial vessel was evacuated, and the desired axial load was placed on the sample. While a constant axial load was maintained, the molten metal was pumped from a reservoir into the test vessel until a fluid pressure of 2 MPa was obtained. Seismic measurements were made at axial effective stresses decreasing from 85 MPa to 1.4 MPa. As used in this paper, effective stress is defined as total applied axial stress minus pore pressure. At each effective stress level, compressional and shear pulse waveforms were collected while the metal was in a molten state. Then, the metal was allowed to solidify under pressure, and pulse waveforms were again collected. The test vessel was then reheated until the metal returned to a molten state, and the load was reduced to the value corresponding to the next lower axial effective stress. This procedure was followed for eight loading decrements. Measurements were made during unloading to avoid trapping metal at higher stresses in voids that may have been open at lower stress.

In these experiments it was found that the Wood's metal intruded the spaces between the ends of the specimens and the triaxial cell pistons. It was therefore necessary to do corresponding measurements on the intact rock to provide reference spectra that also contained the effects of these additional interfaces.

Finally, experiments were performed to ascertain the reproducibility of the received seismic pulses and their spectra. Measurements of arrival times and amplitudes of transmitted compressional and shear pulses were made a total of six times for each stress of 1.4 MPa, and 85 MPa for intact rock specimen E30. Between measurements the setup was disassembled to evaluate the effect on signal reproducibility of alignment, seating, and coupling between transducers and the rock specimen. The received P and S wave pulses were tapered (as described earlier in this section), and a FFT was performed on the tapered pulses. The average values and the standard deviations of the spectral amplitudes at each of several discrete frequencies were calculated for both P and S pulses and are shown in Figures 8*a* and 8*b*. The observed scatter in the typical compressional and shear

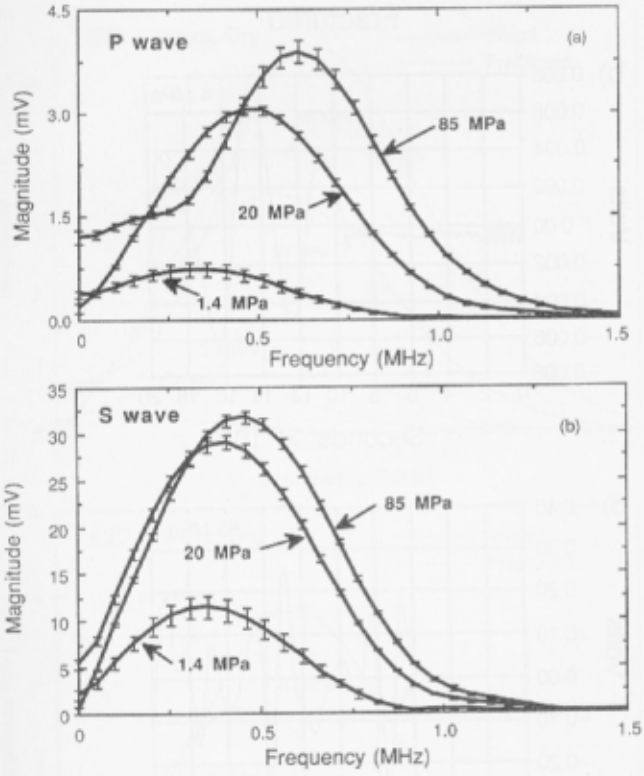

Fig. 8. Averaged results from six measurements at each stress level to evaluate reproducibility of measurements. The length of error bars represents one standard deviation. Shown are the (*a*) *P* wave spectra and (*b*) *S* wave spectra.

pulse spectral data at 85 MPa and 20 MPa is about 7% at the midrange frequencies (0.4–0.6 MHz), decreasing to about 1% at the low and high frequencies. At 1.4 MPa the scatter is about 25% for the midrange frequencies and about 10% at the low and high frequencies. The larger scatter in the spectra at 1.4 MPa for both compressional and shear pulses can be attributed to the uncertainty in the applied load, which at this stress level corresponds to about ±0.7 MPa.

EXPERIMENTAL RESULTS

For all specimens except fractured specimen E32, *P* and *S* wave pulses were collected at axial stresses of 1.4 MPa, 2.9 MPa, 6 MPa, 10 MPa, 20 MPa, 33 MPa, and 85 MPa under both dry and saturated conditions. Data were not collected for fractured specimen E32 at 1.4 MPa under dry conditions. In the sections that follow, results for selected stress levels are shown to illustrate observed trends in the data. Results at stress levels not shown in the figures were compiled by L. J. Pyrak-Nolte (A study of the seismic properties of fractures, unpublished manuscript, 1988) (hereinafter referred to as L. J. Pyrak-Nolte, unpublished manuscript, 1988).

Observed Waveforms

Typical compressional pulse waveforms at axial stresses of 1.4 MPa and 85 MPa for intact and fractured specimens E35 are shown in Figures 9*a*–9*d*. Table 2 summarizes amplitude and travel time data for each of the specimens tested for the lowest and highest values of stress used.

In Figure 9 the first arrival is indicated by an arrow. The "ringing" which occurs in the initial part of the pulse is caused by electromagnetic coupling between cables carrying the high-voltage pulse to the transmission piezoelectric element and the cables connected to the receiving element. The amplitude of this ringing is at most an order of magnitude less than the amplitude of the smallest seismic signal and has a frequency content (over 2 MHz) outside the range of interest in these studies.

Amplitudes listed in Table 2 are the peak-to-peak amplitudes of the first arriving pulse. The geometry of the experiment was chosen to ensure that the first arriving pulse was not contaminated by reflections.

From Figures 9*a*–9*d* and Table 2 it is observed that increasing the axial stress on both the intact and the fractured specimens resulted in larger amplitudes and faster travel times. However, the results show that amplitudes were much more sensitive to changes in stress than the travel times. For example, for intact specimen E35 the compressional wave amplitudes increased by a factor of about 10 between 1.4 MPa and 85 MPa while travel times decreased by 17% (2.54 μs). Though the percentage change in amplitude and travel time differ for the different specimens and between *P* and *S* waves, amplitudes always change much more than travel times. In addition to altering travel times and signal amplitudes, Figure 9 also shows that increasing stress resulted in significant increases in the high-frequency content of the transmitted pulses.

Increases in amplitudes and decreases in travel times of the seismic pulses were greater for the fractured specimens than for the intact specimens. For example, for fractured specimen E35 over the axial stress range of 1.4–85 MPa, there was a decrease in travel time of 20% as opposed to 17% for the intact specimen. The peak-to-peak amplitude of the pulse transmitted through the fractured specimen increased by a factor of 50, which is 4 times the increase seen for the intact specimen over this range of stresses.

Some changes in velocities and amplitudes can be attributed to the system and, especially, the contacts between the seismic transducers and the specimens. Even the aluminum specimen exhibited changes in signal amplitude and travel time in response to changing axial stress, but the changes were very much smaller than those observed for the rock specimens. We believe these results were due to the imperfect transmission across imperfect contacts among the steel loading piston, the lead foil, and the faces of the aluminum specimens. This is the same mechanism as that which causes amplitude loss and velocity changes in a wave propagating across a fracture.

P Wave Spectra

Figures 10*a*–10*c* contain the *P* wave spectra for seismic pulses transmitted through intact and fractured rock specimens E35, E30, and E32 (for dry condition) for the selected stresses of 2.9 MPa, 20 MPa, and 85 MPa.

As the stress was increased on both the intact and the fractured rock specimens, increases in spectral amplitudes were observed, together with a shift in the frequency of the peak amplitudes toward higher frequencies.

The important difference between the spectra for the intact and those for the fractured specimens is that at low stresses, the spectral amplitudes for the fractured specimens were much lower than those for the intact specimens at the same stress levels. This behavior can be explained by the

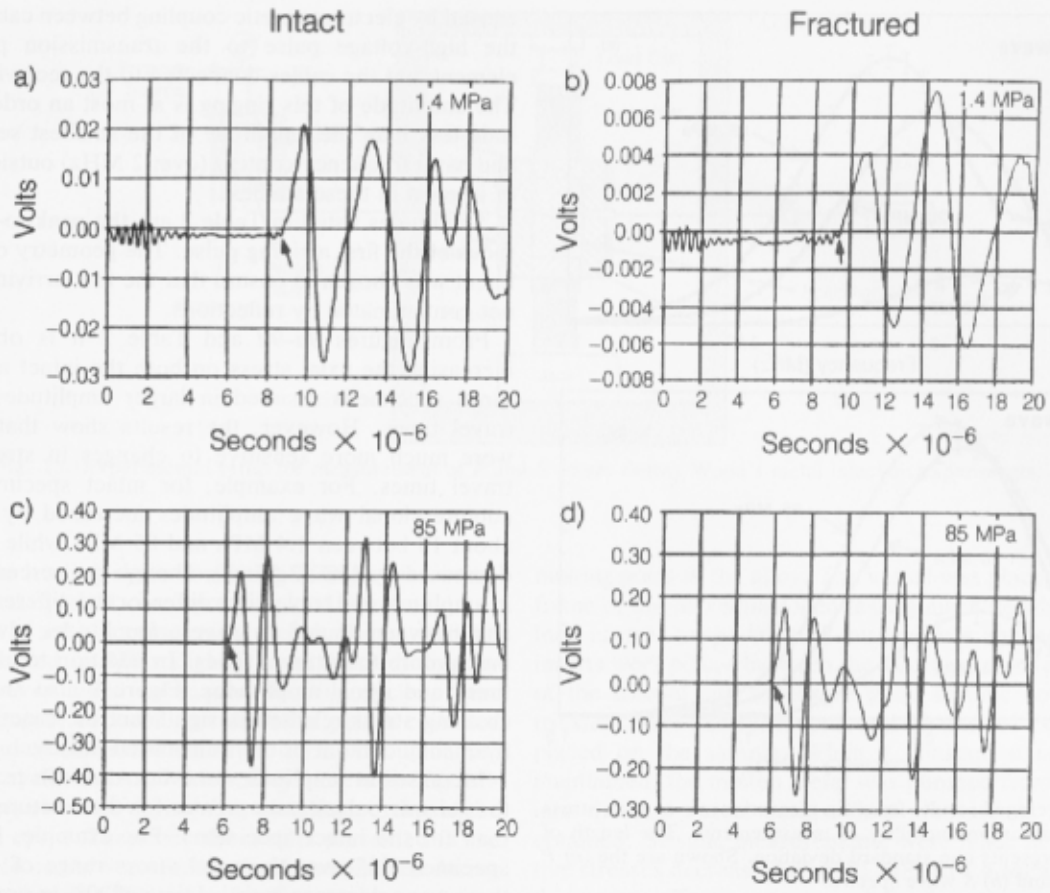

Fig. 9. Comparison of received *P* wave pulses at an axial stress of 1.4 MPa for (*a*) intact and (*b*) fractured specimen E35 and at an axial stress of 85 MPa for (*c*) intact and (*d*) fractured specimen E35. Measurements were made under dry conditions.

displacement discontinuity model. At low stresses the displacement discontinuities caused by the fracture have low values of specific stiffness. As a consequence, a portion of the seismic pulse is reflected by the fracture, resulting in spectral amplitudes that are lower for the pulses transmitted across the fracture than for those transmitted through the intact rock. As stress on the fracture increases, the specific stiffness of the displacement discontinuity increases. Consequently, the effect of the fracture on the amplitudes of the transmitted pulses also diminishes. If the specific stiffness is high enough, the fractures will transmit almost all the energy in the pulse. Thus, for example, as shown in Figure 10*b*, for sample E30 at 85 MPa the spectra of the pulse transmitted through the fractured specimen was virtually the same as that transmitted through the intact specimen.

The differences in the seismic behavior among the three fractured specimens can be explained by the differences in the specific stiffnesses of the fractures. For example, at 85 MPa, fractured specimen E30 transmitted pulses as well as the intact specimen, but at the same stress level fractured specimen E35 transmitted significantly less energy than the intact specimen. The reason for this is evident in Figure 1, where the specific stiffness of the fracture in specimen E35 remained low compared to the fracture in specimen E30,

TABLE 2. Amplitude and Travel Time Data for Specimens Tested Under Dry Conditions

Specimen	Axial Stress, MPa	*P* Wave, Intact Specimens		*S* Wave, Intact Specimens		*P* Wave, Fractured Specimens		*S* Wave, Fractured Specimens	
		Amplitude, mV	Travel Time, μs	Amplitude, mV	Travel Time, μs	Amplitude, mV	Travel Time, μs	Amplitude, mV	Travel Time, μs
E35	1.4	47	15.31	680	23.50	9	15.68	72	25.37
	85	580	12.77	2650	20.47	450	12.65	1110	21.85
E30	1.4	37	14.47	350	24.74	18	14.66	145	24.43
	85	430	12.87	2025	22.42	410	13.07	1850	22.55
E32*	2.9	60	14.94	860	25.41	43	13.98	340	22.99
	85	460	13.28	2700	22.90	480	12.79	2700	22.56

Amplitudes are peak-to-peak amplitudes of the first arrival pulse. Travel times are the travel times through the specimens.
*For fractured specimen E32, the lowest stress level at which data was taken was 2.9 MPa.

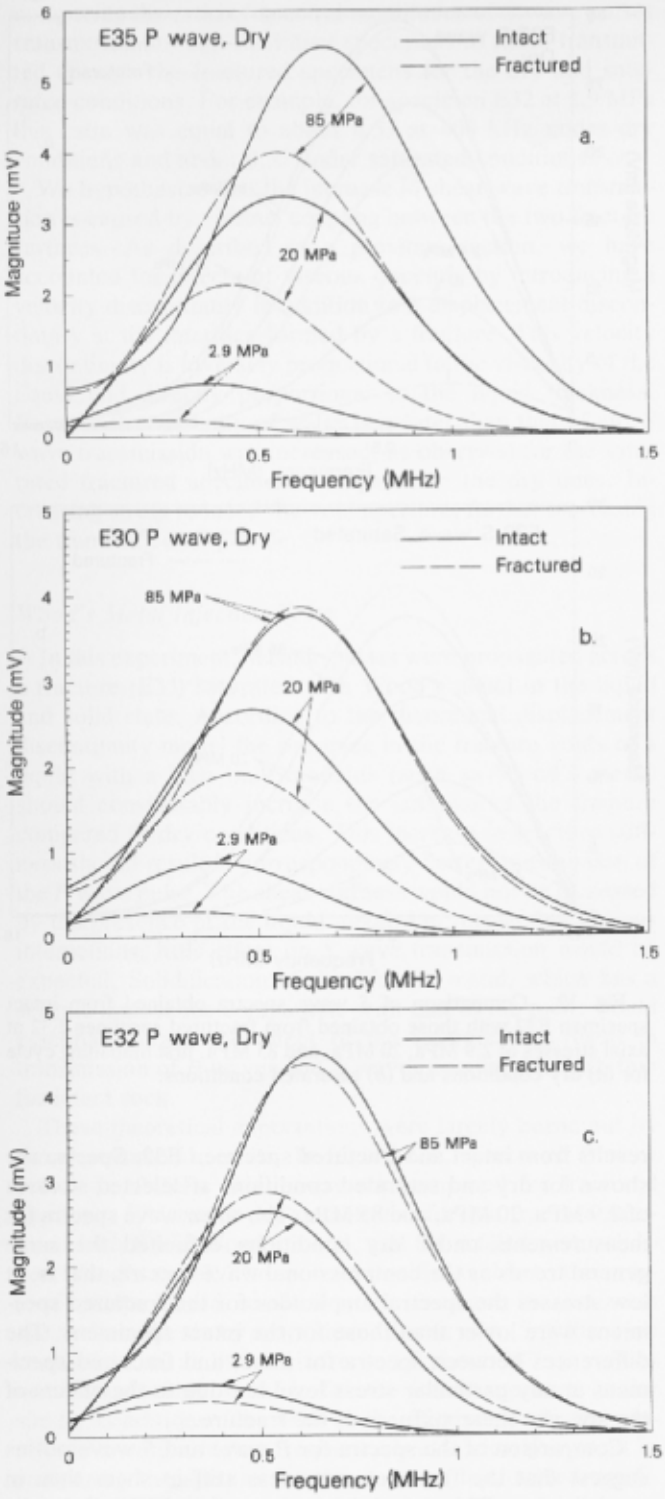

Fig. 10. Comparison of P wave spectra obtained from intact specimens with those obtained from fractured specimens at axial stresses of 2.9 MPa, 20 MPa, and 85 MPa, first unloading cycle, dry conditions for (*a*) E35, (*b*) E30, and (*c*) E32.

even at a stress level of 85 MPa. Results in Figure 10*c* for specimen E32, on the other hand, show that at a stress of 20 MPa the fractured specimen transmitted seismic pulses as well as the intact specimen. This is in accord with the specific stiffness illustrated in Figure 1 where the specific stiffness of fracture E32 is greater than that for the other two fractures. Also, the specific stiffness of fracture E32 increased with stress at a faster rate.

Though relative changes in seismic properties of fractures can be discussed in terms of changes in specific stiffness as measured in static loading tests, the numerical values of specific stiffnesses are not necessarily equal under static and dynamic loading conditions. This will be discussed further in a later section of this paper.

The effect of saturation on P wave transmission across the fractures can be seen by comparing the relative changes in spectra for the fractured and intact specimens under dry and saturated conditions. Figures 11*a*–11*c* show the spectra of the transmitted P wave pulses for intact and fractured rock specimens E35, E30, and E32 under saturated conditions for the selected stresses of 2.9 MPa, 20 MPa, and 85 MPa. At low stress levels the ratio of spectral amplitudes for fractured specimens to those for intact specimens was higher for the saturated specimens than for the dry specimens. (This ratio equals 1 if the fracture transmits as well as the intact rock.) For example, for specimen E30 this ratio was about 0.46 at 500 kHz under saturated conditions, compared to about 0.27 under dry conditions.

These differences between saturated and dry fracture behavior show the increased fracture stiffness resulting from the water in the fracture voids. As a P wave propagates across a saturated fracture, the dynamic load will be distributed between the water in the voids and the solid asperities of contact. The deformation of the fracture, and hence its specific stiffness, are thus affected by the presence of the water. The degree to which a saturated fracture will be stiffened depends on the area and aperture of the voids. Comparison of the spectra under dry and saturated conditions for specimens E30 and E32 from Figures 10 and 11 show that the spectral amplitudes of the fractured specimens and the intact specimens became similar (spectral ratios nearly equal to 1) as stress across the fracture increased. Increasing stress reduced the area of open voids, leading to increased specific stiffness of the fracture. At high stress the percentage of void space was low enough and the specific stiffness was high enough that the additional stiffness provided by water in the remaining voids had little effect on the transmitted wave. Since the fracture specific stiffness was increased at low stresses but not at high stresses, there was also a smaller shift in frequency of the maximum spectral amplitude between 1.4 MPa and 85 MPa for the saturated fractures than for the dry fractures.

In comparison to fractured specimens E30 and E32, fractured specimen E35 exhibited the greatest increase in spectral amplitudes in response to the presence of water, and the increases were observed even at high stresses. The low value of specific stiffness for fractured specimen E35 suggests that the percentage of void space remained high even at high stress levels. Thus it would be reasonable to expect that water in the voids would continue to influence the specific stiffness of this fracture at high stresses.

Figures 10 and 11 show that the spectral amplitudes of P wave pulses generally increased upon saturation for both fractured and intact specimens. Exceptions to this trend are seen in the data for intact specimens E35 and E32 which showed a decrease in spectral amplitude under saturated conditions at the highest stresses. A possible explanation is that microcrack dilatation occurred at the highest stresses,

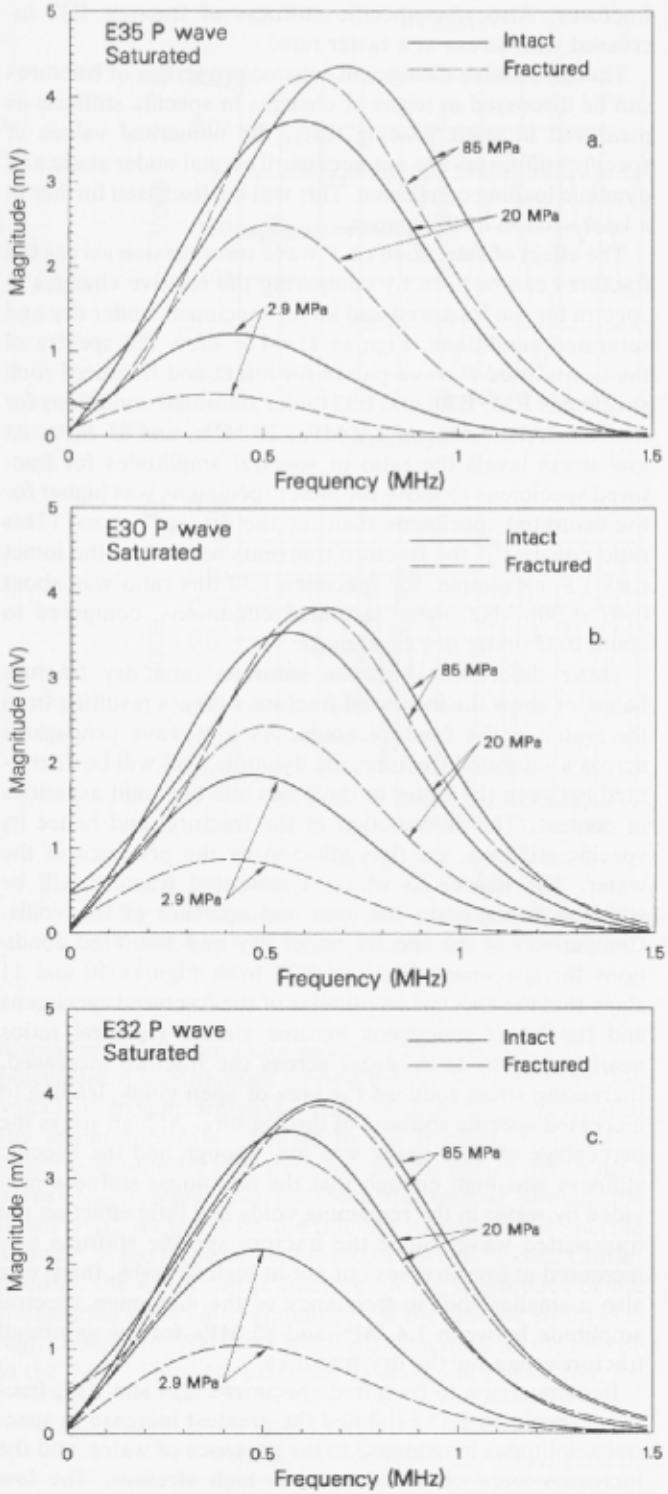

Fig. 11. Comparison of *P* wave spectra obtained from intact specimens with those obtained from fractured specimens at axial stresses of 2.9 MPa, 20 MPa, and 85 MPa, first unloading cycle, saturated conditions for (*a*) E35, (*b*) E30, and (*c*) E32.

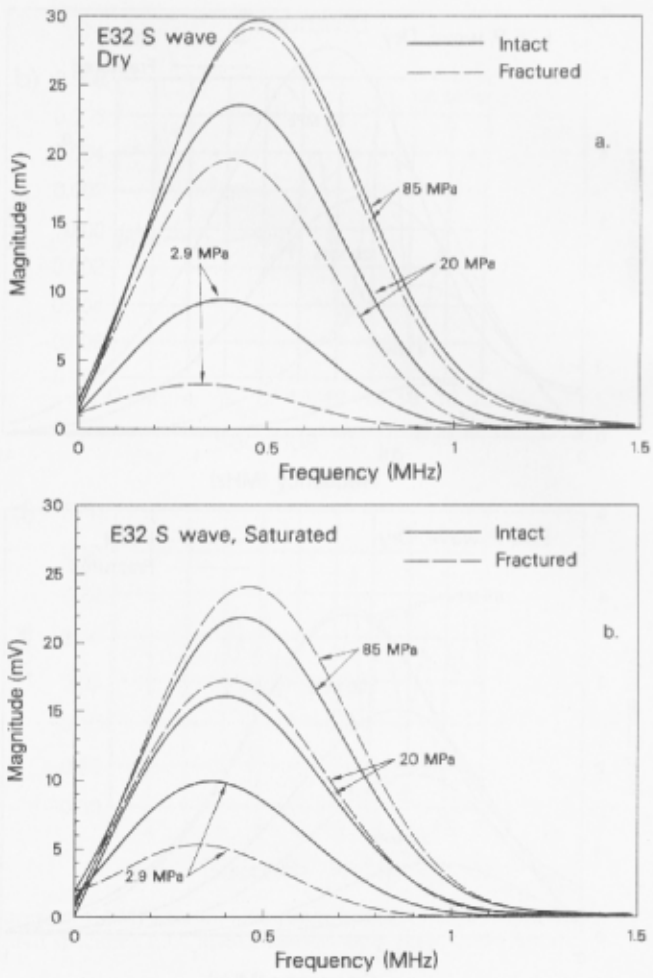

Fig. 12. Comparison of *S* wave spectra obtained from intact specimen E32 with those obtained from fractured specimen E32 at axial stresses of 2.9 MPa, 20 MPa, and 85 MPa, first unloading cycle for (*a*) dry conditions and (*b*) saturated conditions.

leading to partial saturation and permitting energy dissipation by "squirting flow" [*Mavko and Nur*, 1979].

S Wave Spectra

The effect of a single fracture on spectra of the transmitted *S* wave pulses is illustrated in Figures 12*a* and 12*b* using the results from intact and fractured specimen E32. Spectra are shown for dry and saturated conditions at selected stresses of 2.9 MPa, 20 MPa, and 85 MPa. The shear wave spectra for measurements under dry conditions exhibited the same general trends as the compressional wave spectra, that is, at low stresses the spectral amplitudes for the fractured specimens were lower than those for the intact specimens. The differences between spectra for intact and fractured specimens at any particular stress level are due to the effects of the specific shear stiffness of the fracture.

Comparison of the spectra for *P* wave and *S* wave pulses suggest that the fractures were less stiff in shear than in compression. This trend is most easily observed in the results for specimens E32. Nearly 100% transmission of the *P* wave pulse in the fractured specimen occurred at a stress of 20 MPa or less, while full transmission of the *S* wave pulse for this fracture did not occur until a stress of 85 MPa was approached.

Because water has no shear stiffness, it might be anticipated that saturation of the fracture would have little effect on transmission of the shear wave. However, this was not observed. For all fractured specimens, at low to intermediate stress the saturated fractures transmitted more *S* wave energy than the dry fractures. This trend can be seen by

comparing the ratio of spectral amplitudes of S wave pulses transmitted through the intact specimens to those transmitted through the fractured specimens for the dry and saturated conditions. For example, for specimen E32 at 2.9 MPa this ratio was equal to about 0.33 at 400 kHz under dry conditions and about 0.55 under saturated conditions.

We hypothesize that the increase in shear wave transmission is caused by viscous coupling between the two fracture surfaces. As described in a previous section, we have accounted for effects of viscous coupling by introducing a velocity discontinuity in addition to a displacement discontinuity at the interface formed by a fracture. This velocity discontinuity is inversely proportional to the viscosity of the liquid and directly proportional to the liquid thickness. Because the viscosity of water is greater than that of air, S wave transmission was increased, as observed for the saturated fractured specimens compared to the dry ones. Increasing stress reduced the void aperture, further increasing the transmitted amplitude.

Wood's Metal Injection Tests

In this experiment, seismic pulses were propagated across a fracture (E35) saturated with Wood's metal in the liquid and solid state. According to the theoretical displacement discontinuity model the presence in the fracture voids of a liquid with a high bulk modulus (such as Wood's metal) should considerably increase the stiffness of the fracture compared to dry conditions. This increase in fracture stiffness should result in correspondingly better transmission of the P wave pulse. The shear stiffness would not be increased by the presence of the liquid metal, i.e., neglecting viscous interactions, little effect on S wave transmission would be expected. Solidification of the Wood's metal, which has a seismic impedance comparable with that of the rock, would essentially erase the effect of the fracture and result in transmission of P waves and S waves comparable with that for intact rock.

These theoretical expectations were largely borne out by the experimental results. In Figure 13*a*, spectra of P wave pulses at 10 MPa axial stress are compared for fractured specimen E35 under dry conditions, for the fracture saturated with liquid Wood's metal, and for it filled with solidified Wood's metal. The increased stiffness due to the presence of the liquid resulted in an increase in maximum spectral amplitude by more than a factor of 6. Solidification resulted in an additional increase of about 38% to values nearly equivalent to those for the intact specimen under similar conditions. The shift of the maximum spectral amplitude toward a higher frequency is also clearly evident in comparing the spectra for the dry and liquid-filled conditions. Solidification resulted in a slight shift toward lower frequencies, perhaps because of a decrease in "pumping losses" which would occur as the liquid metal flowed between voids in response to the seismic stresses. Measurements at other stresses (L. J. Pyrak-Nolte, unpublished manuscript, 1988) were similar though the difference between results under dry and those under liquid Wood's metal filled conditions diminished at high stresses as would be expected.

In Figure 13*b* spectra of S wave pulses are compared for fractured specimen E35 for the same conditions shown in Figure 13*a*. The maximum spectral amplitude for the liquid-metal-saturated test is about 60% higher than for the test under dry conditions. This effect is much less than that observed for the P waves (Figure 13*a*). Upon solidification of the metal, however, the peak spectral amplitude increased again by about a factor of 4, showing the increase in shear stiffness due to the solidified metal. The S wave spectra for the test with solidified metal in the fracture were essentially the same at all stress levels as those obtained for the intact specimen.

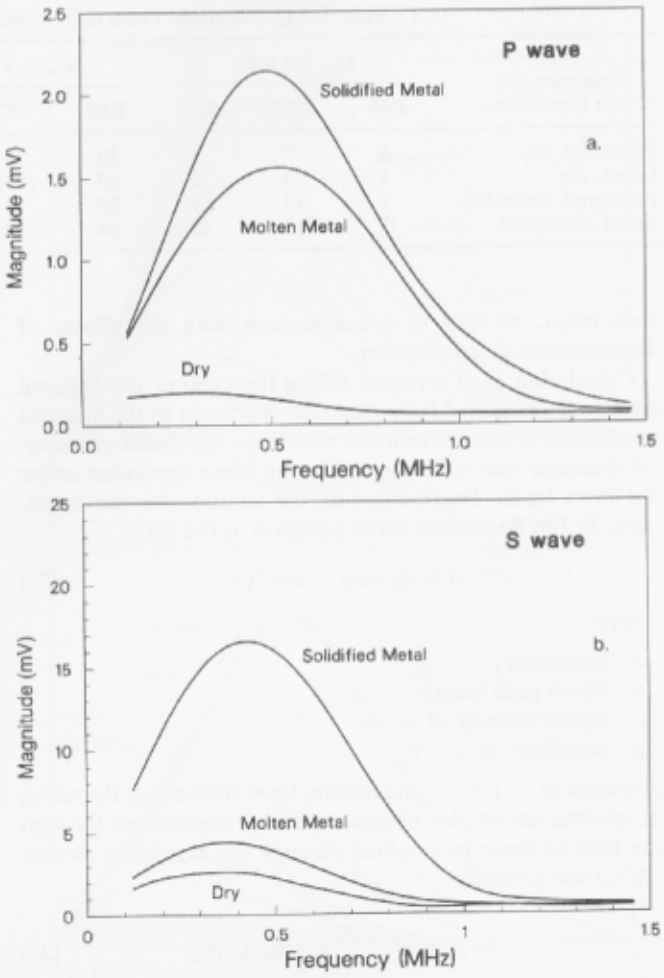

Fig. 13. Comparison of spectra obtained from fractured specimen E35 at an axial stress of 10 MPa under dry conditions, with molten Wood's metal in the fracture voids, and with solidified Wood's metal in the fracture voids for the (*a*) P wave and (*b*) S wave.

Seismic Q Analysis

The seismic quality factor Q is often used as a measure of wave attenuation in materials. We calculated Q for both the intact and the fractured specimens as another measure of the apparent attenuation across a fracture relative to that in the intact rock. The equations for calculations of Q include a length term, so, strictly speaking, the analysis for the fractured specimens pertains only to a rock with a fracture density of one fracture per 77 mm. Nevertheless, the analysis provides a basis for a discussion of the kind of frequency dependence for Q which might be expected in a fractured

TABLE 3. Q Calculated From (23) for All Specimens at Selected Axial Stress Levels

Specimen and Test Conditions	Q_p, 2.9 MPa			Q_s, 2.9 MPa			Q_p, 20 MPa			Q_s, 20 MPa		
	E30	E32	E35	E30	E32	E35	E30	E32	E35	E30	E32	E35
Fractured, dry	8	9	7	22	18	12	17	24	14	25	40	23
Intact, dry	8	9	12	29	33	32	20	24	39	32	51	71
Fractured, saturated	8	17	9	27	19	28	25	36	30	30	40	39
Intact, saturated	17	18	15	34	29	41	37	36	51	45	40	56

rock mass, as well as a comparison with the effects of displacement discontinuities.

Calculation of Q involves taking the ratio of the spectral amplitudes obtained from the rock specimen to the spectral amplitudes obtained from the aluminum specimen of identical diameter and length tested in the same apparatus under the same loads. Beginning with the solution for the amplitudes in the dispersive wave equation in the form

$$A = A_0 \exp(-\omega x/2Qc) \tag{22}$$

where

ω frequency;
x travel path length;
c phase velocity of wave;
A_0 amplitude at $x = 0$.

Johnston et al. [1979], and others, have shown that the ratios of spectral amplitudes of seismic pulses transmitted through the rock to those transmitted through the aluminum sample (A/A_l) are given by

$$\ln A/A_l = -\frac{\pi f x}{Qc} + \ln A_0/A_{0l} \tag{23}$$

where $f = \omega/2\pi$.

In arriving at this result, it is assumed that the Q of aluminum is much greater than the Q of the rock. (Cited values of Q for aluminum range from 2900 to 200,000 at frequencies between 1 kHz and 68 MHz [*Johnston*, 1981].) Equation (23) predicts that the plot of the natural log of spectral ratios as a function of frequency should be a straight line. For both the intact and the fractured rock specimens these plots were linear only for the limited band of about 0.4–0.6 MHz. Values of Q for P waves (Q_p) and S waves (Q_s) obtained from data over this frequency range are listed in Table 3 for each intact and fractured sample under dry and saturated conditions at the effective stress levels 2.9 MPa and 20 MPa. Calculated values of Q at 10 MPa and 85 MPa substantiated these trends (L. J. Pyrak-Nolte, unpublished manuscript, 1988).

Several trends can be observed in comparing values of Q in Table 3 for the different specimens and test conditions. First, Q_p and Q_s increased as axial stress increased on both intact and fractured specimens. Second, Q values for fractured specimens were lower or equal to those for the intact specimens under dry conditions at all stresses. Third, saturation of the fractures resulted in higher values of Q_p and Q_s at the same stress states, consistent with the changes in spectral amplitudes discussed earlier. The rank correlation between fracture stiffness and attenuation is seen in comparing Q for P waves for the three fractured specimens; E35 had the lowest Q, E30 the intermediate value, and E32 the highest value.

Because of the nonlinearity in the spectral ratio data an alternative method was adopted for the calculation of Q. It was assumed that the term (A_0/A_{0l}) in (23) was equal to 1. Rearranging terms, Q is then given by

$$Q = -\pi f x/[c \ln (A/A_l)] \tag{24}$$

This equation was used to calculate values of Q as a function of frequency. A typical result is shown in Figure 14*a*, in which $1/Q$ is plotted as a function of frequency for E30 intact and fractured specimens under dry conditions. For comparison, the values of $1/Q$ obtained using (23) over a frequency range of 0.4–0.6 MHz are plotted as circles in the figure. At 2.9 MPa and 10 MPa the $1/Q$ curve for the fractured

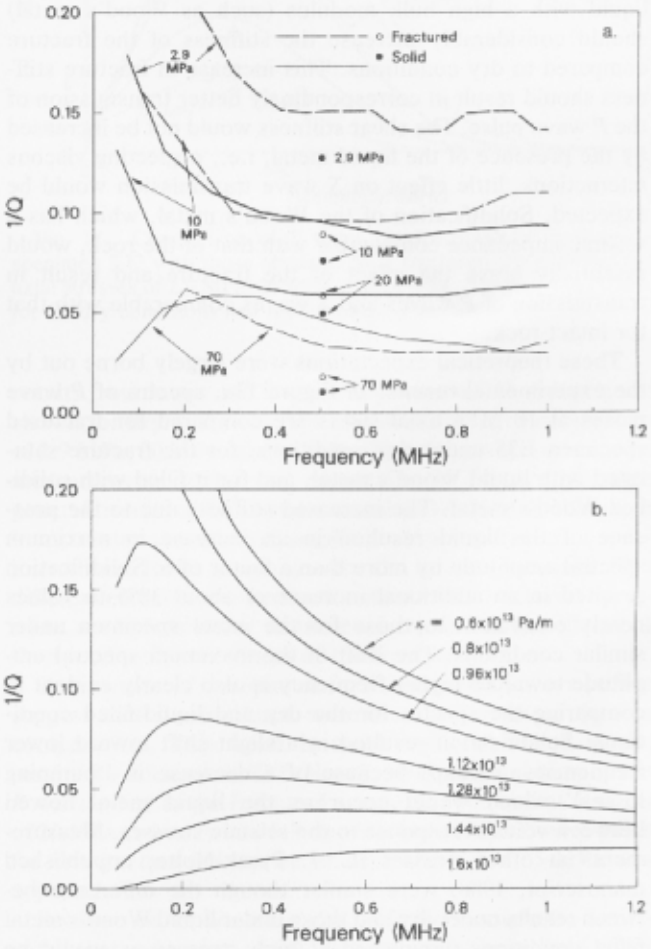

Fig. 14. (*a*) Values of $1/Q$ as a function of frequency for intact and fractured specimens E30, dry condition, obtained using (24). Open circles and solid circles are values of $1/Q$ obtained using (23). (*b*) Theoretical $1/Q$ curves for a range of stiffnesses and for a fractured but otherwise lossless medium are also shown.

specimen is higher than the curve for the intact specimen, showing greater apparent loss of energy caused by the fracture. At 70 MPa the $1/Q$ curves lie one upon the other. However, the most significant feature of the curves in this figure is that the shapes of the curves are very similar for the intact and fractured specimens. The similarity in shape between the curves suggests that the microcracks in the intact specimen were behaving in a manner similar to that of the macroscopic fracture in the fractured specimen. An additional evaluation of this hypothesis was carried out by calculating values of $1/Q$ using (24) and substituting theoretical values of $|T|$ from (16*a*) for (A/A_I). This represents the results of an analysis of Q for a hypothetical experiment in which attenuation of a wave is caused by fractures with a density of one fracture per 77 mm in an otherwise lossless medium. It is assumed that the fracture is represented by a displacement discontinuity with stiffness varying from 6.4×10^{12} Pa/m to 1.6×10^{13} Pa/m and that the medium has an acoustic impedance equal to that of Stripa granite. The resulting curves of $1/Q$, plotted in Figure 14*b*, are very similar to those obtained from analysis of the experimental data (Figure 14*a*).

Discussion

In the previous section we presented results representative of a large data set from the laboratory investigation of seismic wave propagation across natural fractures in crystalline rock. We found that the seismic response of natural fractures under different effective stresses could be explained, qualitatively, by the displacement discontinuity model of wave transmission across a nonwelded interface.

To make a quantitative comparison between theoretical and experimental results, amplitude spectra for the fractured specimens were predicted using the displacement discontinuity theory and compared with those observed experimentally. To obtain predicted spectra for seismic pulses transmitted across the fractures, the experimentally observed spectra for the intact rock specimens at every stress were multiplied by values of the magnitude of the transmission coefficients given in (16*a*), using the rock properties given in Table 1 and values of dynamic specific stiffnesses determined by trial and error to give the "best fit." The term "dynamic specific stiffness" is used to differentiate between the values of specific stiffness obtained from the seismic measurements and those obtained from static measurements. The best fit values for dynamic specific stiffness were determined from a linear regression of the plot of predicted spectral amplitudes versus measured spectral amplitudes. (A perfect fit would result in a slope of 1, an intercept of zero, and a correlation coefficient of 1.00).

Figures 15*a*–15*c* show predicted and measured spectra of *P* wave pulses for fractured rock specimens E35, E32, and E30 in the dry condition at all axial stresses at which measurements were made. Figures 16*a*–16*c* compare predicted and measured spectra of *P* wave pulses under saturated conditions. Values of dynamic specific stiffness determined by the fitting process described above are summarized for the various test conditions in Table 4.

Good agreement is obtained between observed and predicted results. The correlation coefficients obtained from the regression analysis ranged from 0.94 to 1.00 for all stresses except 1.4 MPa, for which they ranged from about 0.78 to 0.98. In general, the greatest mismatch between the predicted and the observed amplitudes occurs at frequencies less than the maximum amplitude frequency. Also, the mismatch is greater for the saturated tests than it is for the dry tests.

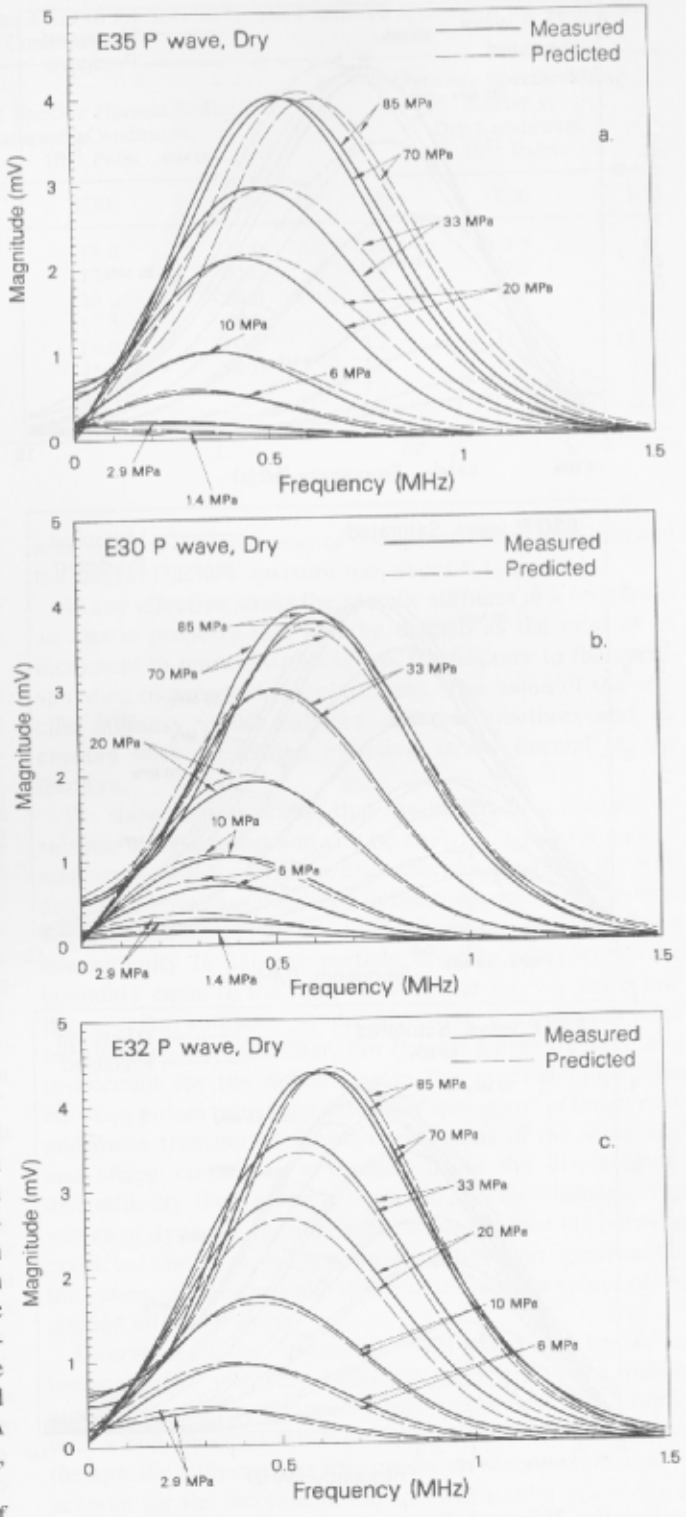

Fig. 15. Measured *P* wave spectra obtained from fractured specimens and predicted spectra at axial stresses from 1.4 MPa to 85 MPa under dry conditions for (*a*) E35, (*b*) E30, and (*c*) E32.

Apart from these discrepancies the theoretical model

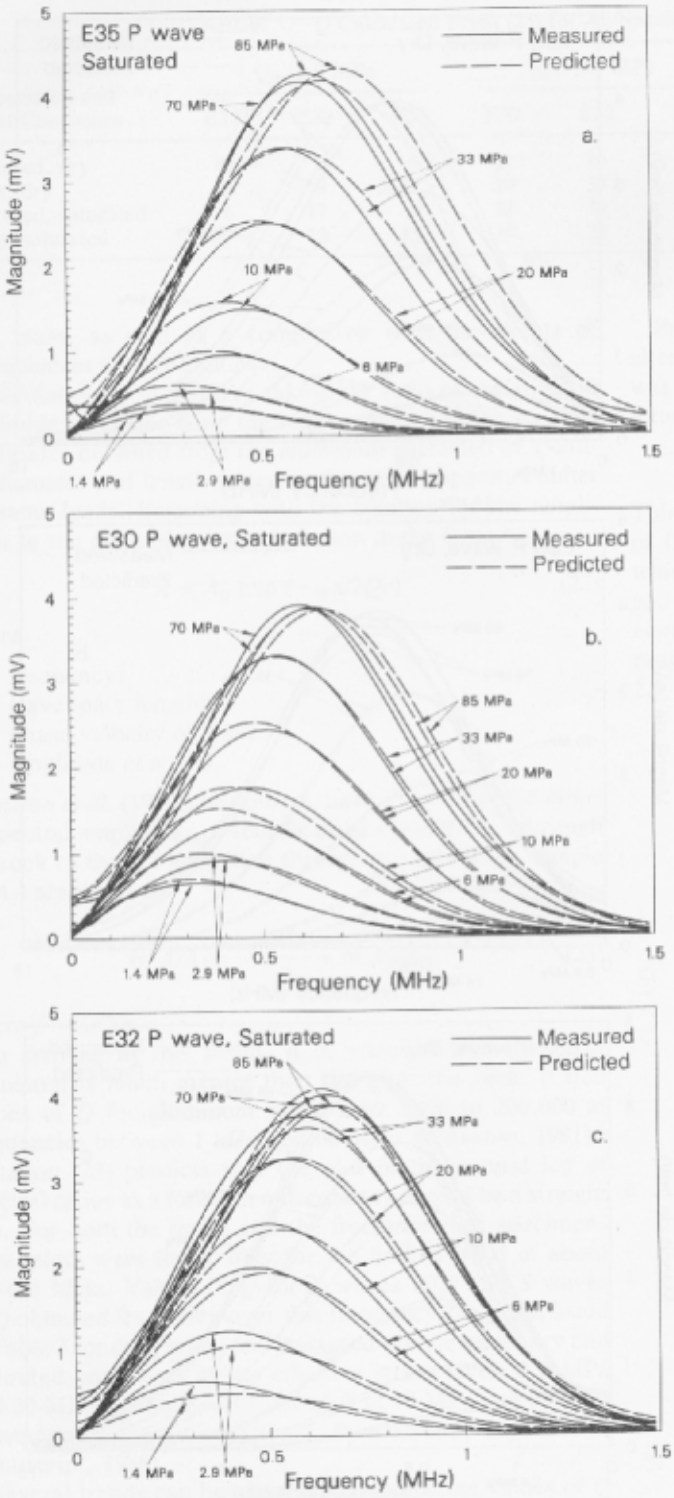

Fig. 16. Measured P wave spectra obtained from fractured specimens and predicted spectra at axial stresses ranging from 1.4 MPa to 85 MPa under saturated conditions for (*a*) E35, (*b*) E30, and (*c*) E32.

matches well the changes in spectra resulting from the effects of changing test conditions. The theoretical curves simulate both the increase in spectral amplitudes as the specific stiffness of the fractures increases with stress and the shift toward higher frequencies of the maximum spectral amplitudes. In comparing the values of dynamic specific stiffness for the three different samples, it is observed that the values are in general greatest for fracture E32 and least for fracture E35, with fracture E30 having intermediate values. Thus the theory predicted the same differences in fracture stiffnesses between samples as observed in the static measurements (Figure 1). Comparison of the dynamic stiffness values for dry and saturated conditions shows that the theory also modeled the increase in stiffness provided by the water in the voids of the saturated fracture. As discussed previously, at high stress levels for specimens E30 and E32 the spectra for fractured and intact specimens were nearly the same. Theoretically, this indicates an infinite fracture specific stiffness as recorded in Table 4. Computationally, it was found that the magnitude of the transmission coefficient was greater than 0.999 at specific stiffness values in excess of 150×10^{12} Pa/m.

Comparison of the values of dynamic specific stiffness given in Table 4 with the static values presented in Figure 1 shows that the values determined from the best fit analyses are of the same order as, but greater than, the static values at all stress levels, and the discrepancy increases at higher stresses. The values of dynamic elastic moduli for rocks are often greater than the corresponding values of the static moduli, perhaps because of frictional effects [e.g., *Jaeger and Cook*, 1979, p. 337]. This same phenomenon seems to affect the values of specific stiffness too.

Figures 17*a*–17*c* show the predicted and measured spectra of S wave pulses for the fractured rock specimens for dry conditions. In general, the agreement is good between observed and predicted results, though discrepancies are noticeable at lower frequencies, particularly for data from measurements at low stresses. Under saturated conditions the mismatch between observed and predicted spectra was worse; using a displacement discontinuity alone resulted in overestimating attenuation of the high-frequency portions of the spectra. The predicted values of dynamic specific shear stiffness for the specimens under dry conditions are given in Table 4. It should be noted that these values are lower than the corresponding values of dynamic specific normal stiffness.

In an attempt to understand the discrepancies between predicted and observed spectra for S wave pulses under saturated conditions, the combined displacement and velocity discontinuity model incorporating both specific stiffness and specific viscosity was used. As can be seen from a comparison of curves in Figure 3, as specific viscosity is increased, the relative attenuation of the high frequencies is decreased. Values of dynamic specific stiffness and specific viscosity were chosen by trial and error until the best fit, determined by regression analysis, was obtained. Figure 18*a* compares observed and predicted S wave spectra for fractured rock specimen E30 under saturated conditions at all axial stresses from 1.4 MPa through 85 MPa; Figure 18*b* shows a comparison of observed and predicted spectra for all three fractured specimens at 6 MPa. It is seen that incorporation of a velocity discontinuity to account for viscous effects together with the elastic displacement discontinuity model results in very good agreement between the observed and the predicted spectra. Correlation coefficients between 0.98 and 1.0 were obtained for predicted shear wave spectra over the entire range of applied stresses for fractured specimen E30. The dynamic specific stiffness and specific viscosity values corresponding to the predicted spectra are

TABLE 4. Values of Dynamic Specific Normal and Shear Stiffness Used to Fit Spectra for All Fractured Specimens Under Dry and Saturated Conditions

Stress, MPa	Dynamic Specific Normal Stiffness, Dry Conditions, 10^{12} Pa/m			Dynamic Specific Normal Stiffness, Saturated Conditions, 10^{12} Pa/m			Dynamic Specific Shear Stiffness, Dry Conditions, 10^{12} Pa/m		
	E35	E30	E32	E35	E30	E32	E35	E30	E32
1.4	2.1	8.2	...	7.9	13.0	15.0	0.95	3.8	...
2.9	4.0	7.4	15.0	9.5	12.0	35.0	1.9	4.5	3.5
6.0	7.6	9.6	30.0	15.0	15.0	60.0	3.5	6.0	6.0
10.0	11.5	11.0	∞	20.0	17.5	80.0	4.8	8.5	9.5
20.0	20.0	24.0	∞	25.0	26.0	100.0	6.2	12.0	17.0
33.0	24.0	43.0	∞	37.0	45.0	200.0	7.0	16.0	35.0
70.0	32.0	∞	120.0	59.0	140.0	∞	7.4	30.0	55.0
85.0	34.0	∞	150.0	200.0	∞	∞	8.0	36.0	60.0

shown in Table 5. Comparison with dynamic specific stiffness values obtained assuming a zero specific viscosity (Table 4) shows that incorporation of viscous effects in the theoretical method led to lower best fit values of dynamic specific stiffness.

Though further work needs to be done, these analyses indicate that viscous coupling between fracture surfaces may contribute to the transmission of shear waves across saturated fractures. If, in general, discrepancies between predicted and observed spectral values at lower frequencies using only the displacement discontinuity are indications of viscous coupling, then this study also suggests that *P* waves and *S* waves under "dry" conditions had a viscous component of coupling across the fracture. For example, as shown in Figure 19 for fractured specimen E30 under dry conditions at axial stresses of 2.9 MPa, 20 MPa, and 85 MPa, observed and predicted *S* wave spectra using a combined displacement and velocity discontinuity are in much better agreement with one another than those in Figure 17*b* based on a discontinuity in displacement only.

The displacement discontinuity model predicts that a fracture will delay as well as attenuate a seismic wave. *Pyrak-Nolte et al.* [1987*b*] used the group time delay predicted by the theory to develop expressions for *P* and *S* wave velocities in a rock containing fractures. They found that the seismic velocities depended upon the frequency of the propagating wave and the specific stiffness of the fractures as well as the density and elastic properties of the intact rock. Good agreement between theoretical predictions and velocities measured in the laboratory on specimen E35 was obtained provided that the effect of frequency on the group delay was taken into account.

CONCLUSIONS

The effects of extensive fractures or other nonwelded contacts on the transmission and attenuation of seismic waves is of considerable fundamental importance and practical interest. We have made careful laboratory measurements of the amplitudes and travel times of compressional and shear pulse propagation across different natural fractures orthogonal to the axes of cylindrical specimens of quartz monzonite, under dry and saturated conditions, for effective stresses up to 85 MPa. The wavelength of the *P* pulse was about 10 mm and that of the *S* pulse was about 7 mm, whereas the diameter of the specimens was 52 mm and the largest fracture aperture was about 0.1 mm.

At any effective stress the specific stiffness of a fracture is an elastic property that may be defined as the ratio of an increment in normal stress across the fracture to the corresponding increment in displacement. The value of the specific stiffness varies between different fractures and increases with increasing effective stress normal to the fracture.

We show, theoretically, that the effects of a fracture on seismic wave propagation can be analyzed by introducing a displacement discontinuity, characterized by a specific stiffness, as a boundary condition in the wave equation. Seismic stress is continuous across such a boundary, but there is a discontinuity in seismic particle displacement across the boundary equal to the ratio between the seismic stress and the specific stiffness. A displacement discontinuity also behaves as a low-pass filter. For *P* wave pulses we were able to account for the differences in the spectral amplitudes between pulses transmitted through specimens of intact rock and those transmitted through specimens of the same size and shape containing a fracture using the displacement discontinuity theory and a dynamic specific stiffness. The values of dynamic specific stiffness for the best fits between predicted and observed spectra were, however, greater than the values of static specific stiffness at the same values of the applied effective stress.

Saturation of the specimens, both intact and fractured, increased the spectral amplitudes of the *P* wave pulses compared with the dry specimens. The presence of a liquid with a bulk modulus much greater than that of air increases the specific stiffness of a fracture by an amount sufficient to account for the increase in the spectral amplitudes of the *P* wave pulses using the displacement discontinuity theory. However, the increase in the spectral amplitudes of the *S* wave pulses transmitted across a saturated fracture compared with dry specimens was not expected. We account for these effects by introducing a discontinuity in seismic particle velocity as another boundary condition in the wave equation. The magnitude of the discontinuity in seismic particle velocities across a fracture is equal to the ratio between the seismic stress and a specific viscosity for the fracture. A velocity discontinuity on its own behaves as a frequency-independent attenuator. We were able to account

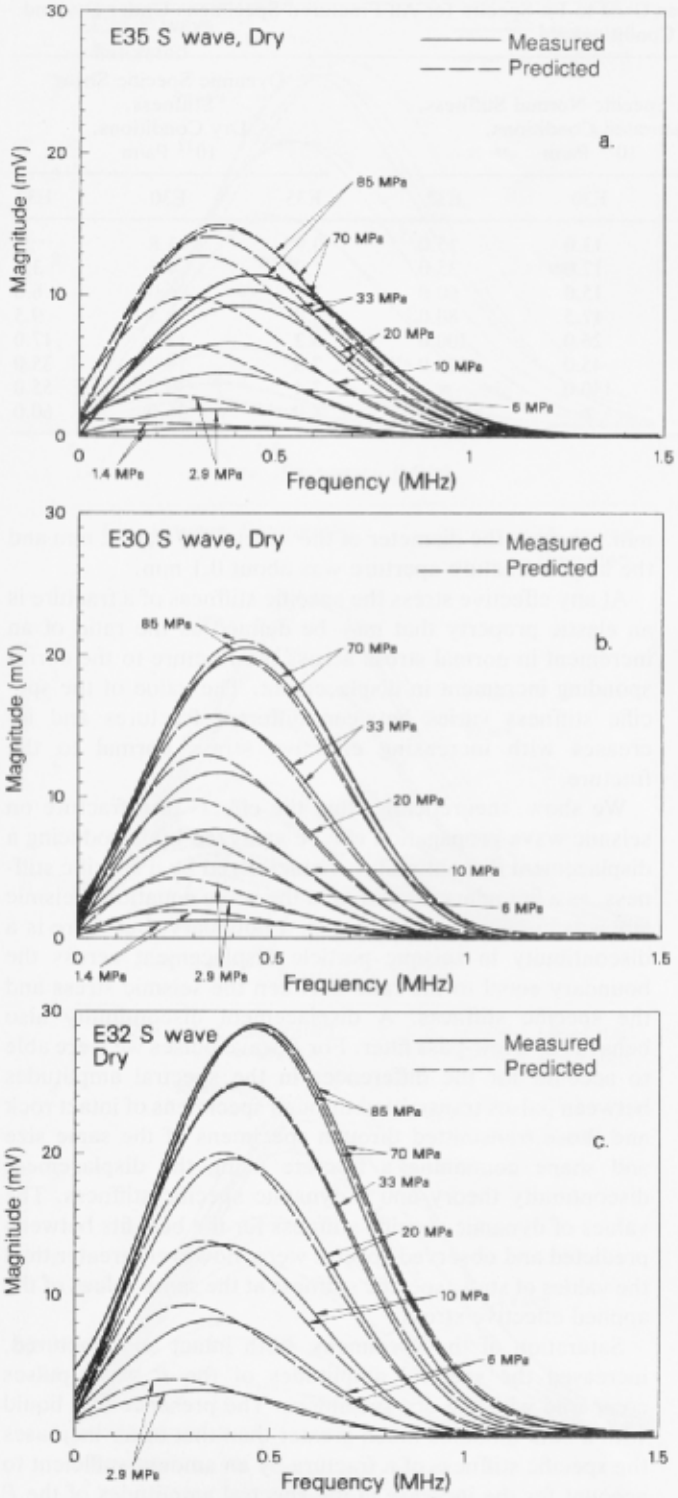

Fig. 17. Measured S wave spectra obtained from fractured specimens and predicted spectra at axial stresses ranging from 1.4 MPa to 85 MPa under dry conditions for (*a*) E35, (*b*) E30, and (*c*) E32.

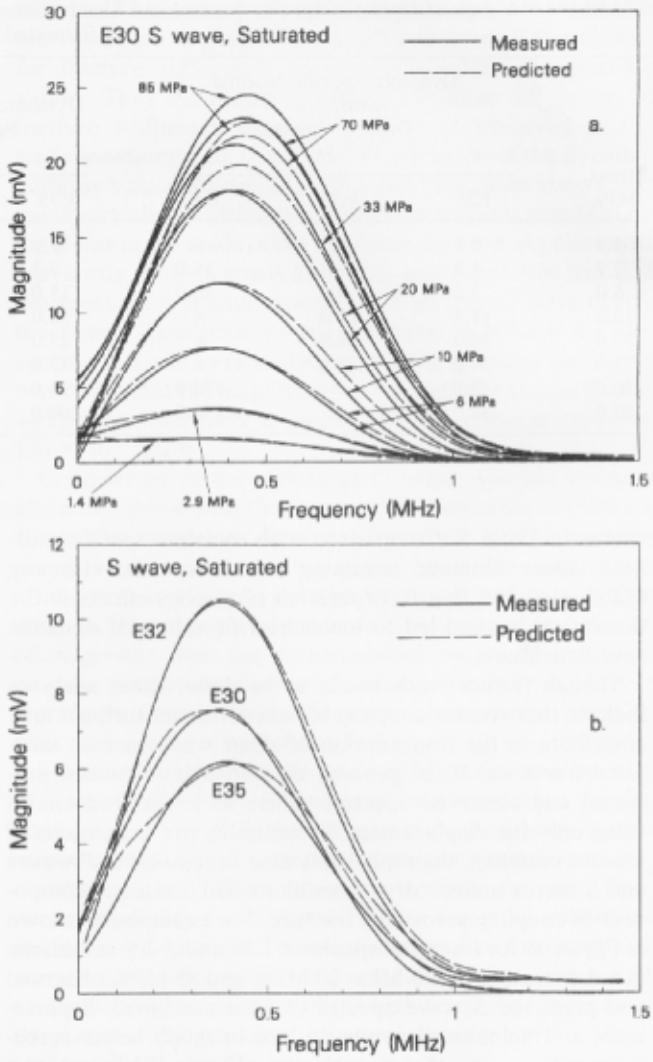

Fig. 18. Comparison of predicted spectra based on both a displacement and a velocity discontinuity with measured S wave spectra; showing (*a*) results for saturated fractured specimen E30 over the axial stress range of 1.4 MPa to 85 MPa and (*b*) comparison of all three saturated fractured specimens at 6 MPa.

for the differences between S wave pulses transmitted through saturated specimens of intact rock and those transmitted through similar specimens containing fractures by using a combined displacement discontinuity and velocity discontinuity with fitted values of dynamic specific stiffness and specific viscosity. The correlation coefficient between theoretical and measured values of spectral amplitudes was always greater than 0.98. However, the viscosity of water is quite insufficient to account for the magnitude of the specific viscosity necessary to achieve the good fits. Furthermore,

TABLE 5. Values of Shear Dynamic Specific Stiffness and of Specific Viscosity Used to Fit S Wave Spectra for Fractured Specimen E30 Under Saturated Conditions Using the Combined Displacement and Velocity Discontinuity Theory

Stress, MPa	Dynamic Stiffness, 10^{12} Pa/m	Specific Viscosity, 10^3 kg/m^{2}s
1.4	1.0	1.3
2.9	2.1	2.1
6.0	5.9	4.0
10.0	14.0	11.0
20.0	60.0	500.0
33.0	∞	···
77.0	∞	···
85.0	∞	···

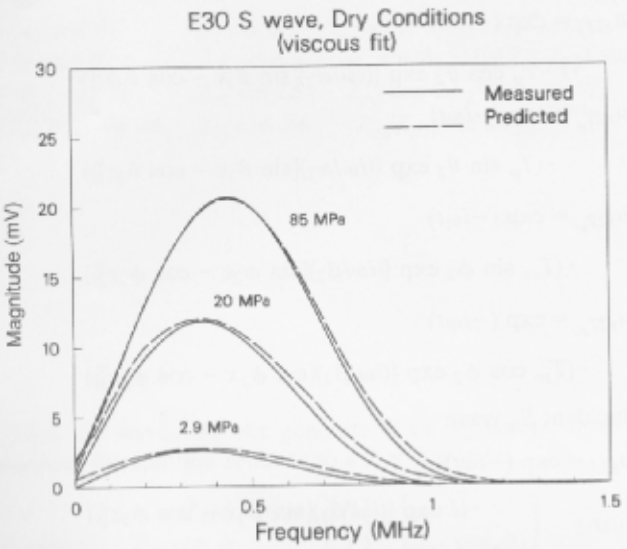

Fig. 19. Comparison of predicted spectra based on both a displacement and a velocity discontinuity with measured S wave spectra obtained from dry fractured specimen E30 at axial stresses of 2.9 MPa, 20 MPa, 20 MPa, and 85 MPa.

better fits between observed and predicted spectra for S wave pulses under dry conditions were obtained by using combined displacement and velocity discontinuities. The physics and chemistry of viscous coupling in a fracture remain to be investigated.

We also analyzed the effect of fractures on the spectral amplitudes of seismic pulses transmitted through specimens of intact rock and similar specimens containing fractures in terms of conventional attenuation approximations using a quality factor, Q. The values of Q for rock were found to be of the order of 20. These values increased with increasing effective stress for specimens of both intact and fractured rock; they were lower for specimens with fractures than for intact specimens, and they were a function of frequency. The most remarkable feature, however, was that the functional dependence of Q on frequency appeared to be very similar for both the intact and the fractured specimens. The displacement discontinuity model can be used also to predict changes in amplitude with frequency (or attenuation) for a wave transmitted through fractured rock.

APPENDIX

The converted, reflected, and transmitted components of compressional and shear waves incident on a displacement discontinuity in the x-y plane between two half-spaces with different values of seismic impedance are illustrated in Figures A1a–A1c. For the governing equations and boundary conditions given in the text, the following solutions may be assumed:

Incident P wave

$$u_{z1I} = \exp(-i\omega t) \cdot (-I \cos\theta_1 \exp\{(i\omega/\alpha_1)[\sin\theta_1 x - \cos\theta_1 z]\})$$

$$u_{x1I} = \exp(-i\omega t) \cdot (I \sin\theta_1 \exp\{(i\omega/\alpha_1)[\sin\theta_1 x - \cos\theta_1 z]\})$$

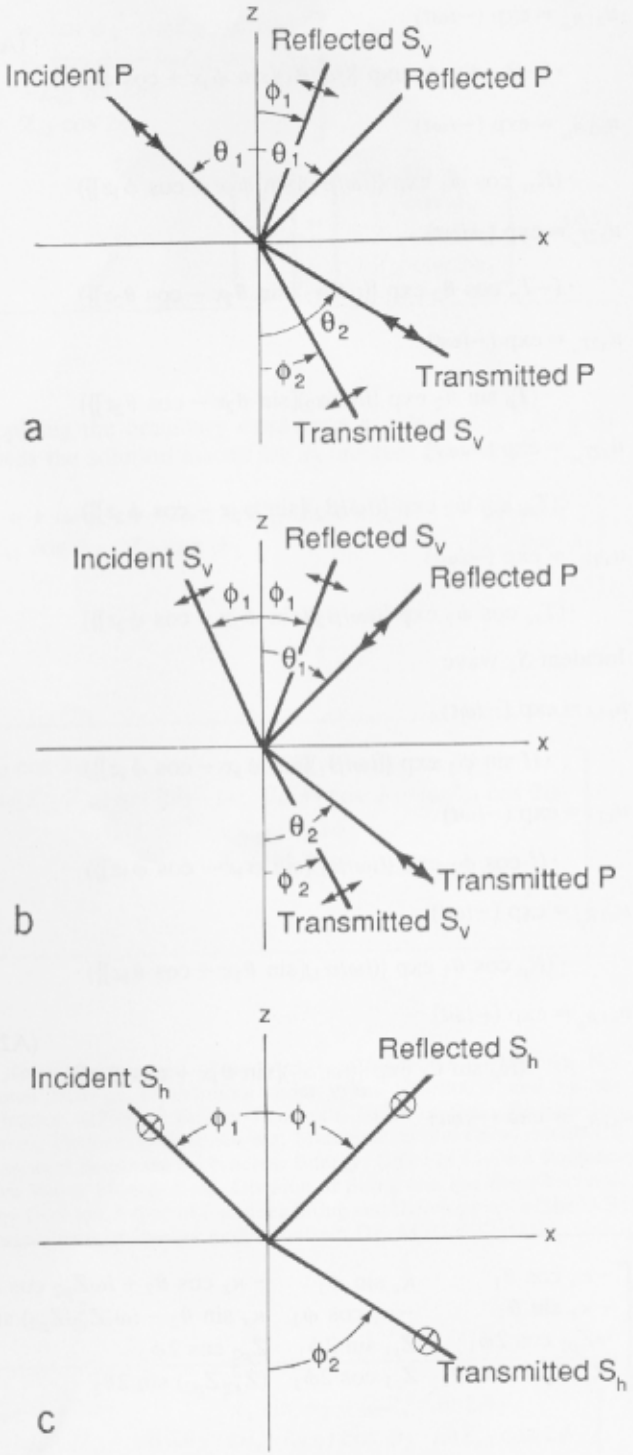

Fig. A1. Converted, reflected, and transmitted components of waves incident on a displacement discontinuity: (*a*) P wave, (*b*) SV wave, and (*c*) SH wave.

$$u_{z1R_p} = \exp(-i\omega t) \cdot (R_p \cos\theta_1 \exp\{(i\omega/\alpha_1)[\sin\theta_1 x + \cos\theta_1 z]\})$$

$$u_{x1R_p} = \exp(-i\omega t) \cdot (R_p \sin\theta_1 \exp\{(i\omega/\alpha_1)[\sin\theta_1 x + \cos\theta_1 z]\})$$

$$
\begin{aligned}
u_{z1R_{sv}} &= \exp(-i\omega t) \\
&\quad \cdot (-R_{sv} \sin\phi_1 \exp\{(i\omega/\beta_1)[\sin\phi_1 x + \cos\phi_1 z]\}) \\
u_{x1R_{sv}} &= \exp(-i\omega t) \\
&\quad \cdot (R_{sv} \cos\phi_1 \exp\{(i\omega/\beta_1)[\sin\phi_1 x + \cos\phi_1 z]\}) \\
u_{z2T_p} &= \exp(-i\omega t) \\
&\quad \cdot (-T_p \cos\theta_2 \exp\{(i\omega/\alpha_2)[\sin\theta_2 x - \cos\theta_2 z]\}) \\
u_{x2T_p} &= \exp(-i\omega t) \\
&\quad \cdot (T_p \sin\theta_2 \exp\{(i\omega/\alpha_2)[\sin\theta_2 x - \cos\theta_2 z]\}) \\
u_{z2T_{sv}} &= \exp(-i\omega t) \\
&\quad \cdot (T_{sv} \sin\phi_2 \exp\{(i\omega/\beta_2)[\sin\phi_2 x - \cos\phi_2 z]\}) \\
u_{x2T_{sv}} &= \exp(-i\omega t) \\
&\quad \cdot (T_{sv} \cos\phi_2 \exp\{(i\omega/\beta_2)[\sin\phi_2 x - \cos\phi_2 z]\})
\end{aligned} \tag{A1}
$$

Incident S_v wave

$$
\begin{aligned}
u_{z1I} &= \exp(-i\omega t) \\
&\quad \cdot (I \sin\phi_1 \exp\{(i\omega/\beta_1)[\sin\phi_1 x - \cos\phi_1 z]\}) \\
u_{x1I} &= \exp(-i\omega t) \\
&\quad \cdot (I \cos\phi_1 \exp\{(i\omega/\beta_1)[\sin\phi_1 x - \cos\phi_1 z]\}) \\
u_{z1R_p} &= \exp(-i\omega t) \\
&\quad \cdot (R_p \cos\theta_1 \exp\{(i\omega/\alpha_1)[\sin\theta_1 x + \cos\theta_1 z]\}) \\
u_{x1R_p} &= \exp(-i\omega t) \\
&\quad \cdot (R_p \sin\theta_1 \exp\{(i\omega/\alpha_1)[\sin\theta_1 x + \cos\theta_1 z]\}) \\
u_{z1R_{sv}} &= \exp(-i\omega t) \\
&\quad \cdot (-R_{sv} \sin\phi_1 \exp\{(i\omega/\beta_1)[\sin\phi_1 x + \cos\phi_1 z]\}) \\
u_{x1R_{sv}} &= \exp(-i\omega t) \\
&\quad \cdot (R_{sv} \cos\phi_1 \exp\{(i\omega/\beta_1)[\sin\phi_1 x + \cos\phi_1 z]\})
\end{aligned} \tag{A2}
$$

$$
\begin{aligned}
u_{z2T_p} &= \exp(-i\omega t) \\
&\quad \cdot (-T_p \cos\theta_2 \exp\{(i\omega/\alpha_2)[\sin\theta_2 x - \cos\theta_2 z]\}) \\
u_{x2T_p} &= \exp(-i\omega t) \\
&\quad \cdot (T_p \sin\theta_2 \exp\{(i\omega/\alpha_2)[\sin\theta_2 x - \cos\theta_2 z]\}) \\
u_{z2T_{sv}} &= \exp(-i\omega t) \\
&\quad \cdot (T_{sv} \sin\phi_2 \exp\{(i\omega/\beta_2)[\sin\phi_2 x - \cos\phi_2 z]\}) \\
u_{x2T_{sv}} &= \exp(-i\omega t) \\
&\quad \cdot (T_{sv} \cos\phi_2 \exp\{(i\omega/\beta_2)[\sin\phi_2 x - \cos\phi_2 z]\})
\end{aligned}
$$

Incident S_h wave

$$
\begin{aligned}
u_{y1I} &= \exp(-i\omega t) \\
&\quad \cdot (I \exp\{(i\omega/\beta_1)[\sin\phi_1 x - \cos\phi_1 z]\}) \\
u_{y1R_{sh}} &= \exp 2(-i\omega t) \\
&\quad 3 \cdot (R_{sh} \exp\{(i\omega 3333333_1)[\sin\phi_1 x + \cos\phi_1 z]\}) \\
u_{y2T_{sh}} &= \exp(-i\omega t) \\
&\quad \cdot (T_{sh} \exp\{(i\omega/\beta_2)[\sin\phi_2 x - \cos\phi_2 z]\})
\end{aligned} \tag{A3}
$$

where I is the amplitude of the incident wave (assumed to be unity in this solution with no loss of generality) and subscriupts 1 and 2 refer to material above and below the displacement discontinuity, respectively. For compressional waves the angle of incidence is θ_1, and the angle of emergence is θ_2. For shear waves the angle of incidence is ϕ_1, and the angle of emergence is ϕ_2. The displacement discontinuity boundary condition does not influence the emergence angles; only the material properties of the elastic half-spaces affect these angles.

Applying the boundary conditions in (9) and (10) to the assumed solutions of (A1) and neglecting the time-dependent term, the solution for an incident P wave, presented in matrix form, is

$$
\begin{bmatrix}
-\kappa_z \cos\theta_1 & \kappa_z \sin\phi_1 & -\kappa_z \cos\theta_2 + i\omega Z_{p2} \cos 2\phi_2 & \kappa_z \sin\phi_2 - i\omega Z_{s2} \sin 2\phi_2 \\
-\kappa_x \sin\theta_1 & -\kappa_x \cos\phi_1 & \kappa_x \sin\theta_2 - i\omega(Z_{s2}^2/Z_{p2}) \sin 2\theta_2 & \kappa_x \cos\phi_2 - i\omega Z_{s2} \cos 2\phi_2 \\
-Z_{p1} \cos 2\phi_1 & Z_{s1} \sin 2\phi_1 & Z_{p2} \cos 2\phi_2 & -Z_{s2} \sin 2\phi_2 \\
(Z_{s1}^2/Z_{p1}) \sin 2\theta_1 & Z_{s1} \cos 2\phi_1 & (Z_{s2}^2/Z_{p2}) \sin 2\theta_2 & Z_{s2} \cos 2\phi_2
\end{bmatrix}
\cdot
\begin{bmatrix} R_p \\ R_s \\ T_p \\ T_s \end{bmatrix}
=
\begin{bmatrix} -\kappa_z \cos\theta_1 \\ \kappa_x \sin\theta_1 \\ Z_{p1} \cos 2\phi_1 \\ (Z_{s1}^2/Z_{p1}) \sin 2\theta_1 \end{bmatrix} \tag{A4}
$$

where Z is the seismic impedance of the half-spaces given by the product of the density and the seismic velocity ($Z_p = \alpha\rho$, and $Z_s = \beta\rho$). For S_v waves the 4×4 matrix is the same as for the incident P wave, but the product matrix is different:

$$\begin{bmatrix} -\kappa_z \cos\theta_1 & \kappa_z \sin\phi_1 & -\kappa_z \cos\theta_2 + i\omega Z_{p2} \cos 2\phi_2 & \kappa_z \sin\phi_2 - i\omega Z_{s2} \sin 2\phi_2 \\ -\kappa_x \sin\theta_1 & -\kappa_x \cos\phi_1 & \kappa_x \sin\theta_2 - i\omega(Z_{s2}^2/Z_{p2}) \sin 2\theta_2 & \kappa_x \cos\phi_2 - i\omega Z_{s2} \cos 2\phi_2 \\ -Z_{p1} \cos 2\phi_1 & Z_{s1} \sin 2\phi_1 & Z_{p2} \cos 2\phi_2 & -Z_{s2} \sin 2\phi_2 \\ (Z_{s1}^2/Z_{p1}) \sin 2\theta_1 & Z_{s1} \cos 2\phi_1 & (Z_{s2}^2/Z_{p2}) \sin 2\theta_2 & Z_{s2} \cos 2\phi_2 \end{bmatrix} \cdot \begin{bmatrix} R_p \\ R_s \\ T_p \\ T_s \end{bmatrix} = \begin{bmatrix} +\kappa_z \sin\phi_1 \\ +\kappa_x \cos\phi_1 \\ -Z_{s1} \sin 2\phi_1 \\ +Z_{s1} \cos 2\phi_1 \end{bmatrix} \quad \text{(A5)}$$

Since S_h waves do not generate P or S_v waves at an interface, the solution reduces to a 2×2 matrix:

$$\begin{bmatrix} -\kappa & \kappa - iZ_{s2}\omega \cos\phi_2 \\ Z_{s1} \cos\phi_1 & Z_{s2} \cos\phi_2 \end{bmatrix} \begin{bmatrix} R \\ T \end{bmatrix} = \begin{bmatrix} \kappa \\ Z_{s1} \cos\phi_1 \end{bmatrix} \quad \text{(A6)}$$

For the case of a viscous interface, applying the boundary conditions in (17) and (18) to (A1) yields the solution matrix for an incident P wave:

$$\begin{bmatrix} -\kappa_z \cos\theta_1 & \kappa_z \sin\phi_1 & -\kappa_z \cos\theta_2 + i\omega Z_{p2} \cos 2\phi_2 & \kappa_z \sin\phi_2 - i\omega Z_{s2} \sin 2\phi_2 \\ (-\kappa_x + i\omega\eta) \sin\theta_1 & (-\kappa_x + i\omega\eta)\cos\phi_1 & (\kappa_x - i\omega\eta) \sin\theta_2 - i\omega(Z_{s2}^2/Z_{p2}) \sin 2\theta_2 & (\kappa_x - i\omega\eta) \cos\phi_2 - i\omega Z_{s2} \cos 2\phi_2 \\ -Z_{p1} \cos 2\phi_1 & Z_{s1} \sin 2\phi_1 & Z_{p2} \cos 2\phi_2 & -Z_{s2} \sin 2\phi_2 \\ (Z_{s1}^2/Z_{p1}) \sin 2\theta_1 & Z_{s1} \cos 2\phi_1 & (Z_{s2}^2/Z_{p2}) \sin 2\theta_2 & Z_{s2} \cos 2\phi_2 \end{bmatrix} \quad \text{(A7)}$$

$$\begin{bmatrix} R_p \\ R_s \\ T_p \\ T_s \end{bmatrix} = \begin{bmatrix} -\kappa_z \cos\theta_1 \\ (\kappa\kappa_x - i\omega\eta) \sin\theta_1 \\ Z_{p1} \cos 2\phi_1 \\ (Z_{s1}^2/Z_{p1}) \sin 2\theta_1 \end{bmatrix} \quad \text{(A8)}$$

For S_v waves, applying the boundary conditions to (A2) yields the same solution matrix as for the incident P wave, but the product matrix is different:

$$\begin{bmatrix} -\kappa_z \cos\theta_1 & \kappa_z \sin\phi_1 & -\kappa_z \cos\theta_2 + i\omega Z_{p2} \cos 2\phi_2 & \kappa_z \sin\phi_2 - i\omega Z_{s2} \sin 2\phi_2 \\ (-\kappa_x + i\omega\eta) \sin\theta_1 & (-\kappa_x + i\omega\eta) \cos\phi_1 & (\kappa_x - i\omega\eta) \sin\theta_2 - i\omega(Z_{s2}^2/Z_{p2}) \sin 2\theta_2 & (\kappa_x - i\omega\eta) \cos\phi_2 - i\omega Z_{s2} \cos 2\phi_2 \\ -Z_{p1} \cos 2\phi_1 & Z_{s1} \sin 2\phi_1 & Z_{p2} \cos 2\phi_2 & -Z_{s2} \sin 2\phi_2 \\ (Z_{s1}^2/Z_{p1}) \sin 2\theta_1 & Z_{s1} \cos 2\phi_1 & (Z_{s2}^2/Z_{p2}) \sin 2\theta_2 & Z_{s2} \cos 2\phi_2 \end{bmatrix} \quad \text{(A9)}$$

$$\begin{bmatrix} R_p \\ R_s \\ T_p \\ T_s \end{bmatrix} = \begin{bmatrix} \kappa_z \sin\phi_1 \\ (\kappa_x i\omega\eta) \cos\phi_1 \\ -Z_{s1} \sin 2\phi_1 \\ Z_{s1} \cos 2\phi_1 \end{bmatrix} \quad \text{(A10)}$$

Applying the boundary conditions in (19) and (20) to (A3) yields the solution matrix for an incident S_h wave:

$$\begin{bmatrix} -\kappa + i\omega\eta & \kappa - i\omega\eta - iZ_{s2}\omega \cos\phi_2 \\ Z_{s1} \cos\phi_1 & Z_{s2} \cos\phi_2 \end{bmatrix} \begin{bmatrix} R \\ T \end{bmatrix} = \begin{bmatrix} \kappa - i\omega\eta \\ Z_{s1} \cos\phi_1 \end{bmatrix} \quad \text{(A11)}$$

Acknowledgments. This work was funded in part by the National Science Foundation under grant EE-830053 and by the Director, Office of Energy Research, Office of Basic Energy Sciences, Division of Engineering, Mathematics and Geosciences and Assistant Secretary for Nuclear Energy, Office of Civilian Radioactive Waste Management, Division of Siting and Facilities Technology Division, Office of Facilities Siting and Development of the U.S. Department of Energy under contract DE-AC03-76SF00098.

REFERENCES

Baik, J.-M., and R. B. Thompson, Ultrasonic scattering from imperfect interfaces: A quasi-static model, *J. Nondestruc. Test.*, *4*(3/4), 177–196, 1984.

Bandis, S. C., A. C. Lumsden, and N. R. Barton, Fundamentals of

rock joint deformation, *Int. J. Rock Mech. Min. Sci. Geomech. Abstr.*, *20*(6), 249–268, 1983.

Cook, N. G. W., and L. R. Myer, Thermomechanical studies at Stripa, Sweden, in *The Science and Technology of the Management of High Level Nuclear Waste*, edited by P. L. Hoffmann and J. Bresline, Office of Nuclear Waste Isolation, Batelle, Columbus, Ohio, 1981.

Crampin, S., A review of wave motion in anisotropic and cracked elastic media, *Wave Motion*, *3*, 343–391, 1981.

Eshbach, O. W., *Handbook of Engineering Fundamentals*, 2nd ed., pp. 1–145, John Wiley, New York, 1952.

Goodman, R. E., *Methods of Geological Engineering*, pp. 170–173, West Publishing, St. Paul, Minn., 1976.

Hudson, J. A., Wave speeds and attenuation of elastic waves in material containing cracks, *Geophys. J. R. Astron. Soc.*, *64*(1), 133–150, 1981.

Jaeger, J. C., and N. G. W. Cook, *Fundamentals of Rock Mechanics*, 3rd ed., Chapman and Hall, London, 1979.

Johnston, D. H., Attenuation: A state-of-the-art summary, in *Seismic Wave Attenuation*, edited by M. N. Toksöz and D. H. Johnston, pp. 123–135, Society of Exploration Geophysics, Tulsa, Okla., 1981.

Johnston, D. H., and M. N. Toksöz, Ultrasonic *P*- and *S*-wave attenuation in dry and saturated rocks under pressure, *J. Geophys. Res.*, *85*, 925–936, 1980.

Johnston, D. H., M. N. Toksöz, and A. Timur, Attenuation of seismic waves in dry and saturated rocks, II, Mechanism, *Geophysics*, *44*(4), 691–711, 1979.

Jones, T., and A. Nur, Velocity and attenuation in sandstone at elevated temperature and pressures, *Geophys. Res. Lett.*, *10*(2), 140–143, 1983.

Kendall, K., and D. Tabor, An ultrasonic study of the area of contact between stationary and sliding surfaces, *Proc. R. Soc. London, Ser. A*, *323*, 321–340, 1971.

King, M. S., L. R. Myer, and J. J. Rezowalli, Experimental studies of elastic-wave propagation in a columnar-jointed rock mass, *Geophys. Prospect.*, *34*(8), 1185–1199, 1986.

Kitsunezaki, C., Behavior of plane elastic waves across a plane crack, *J. Mining Coll. Akita Univ., Ser. A*, *6*(3), 173–187, 1983.

Kjartansson, E., Constant *Q*-wave propagation and attenuation, *J. Geophys. Res.*, *84*, 4737–4748, 1979.

Kleinberg, R. L., E. Y. Chow, T. J. Plona, M. Orton, and W. J. Canady, Sensitivity and reliability of fracture detection techniques for borehole application, *J. Pet. Technol.*, *34*(4), 657–663, 1982.

Kuster, V. T., and M. W. Toksöz, Velocity and attenuation of seismic waves in two-phase media, I, Theoretical formulation, *Geophysics*, *39*(5), 587–606, 1974.

Mavko, G. M., and A. Nur, Wave attenuation in partially saturated rocks, *Geophysics*, *44*(2), 161–178, 1979.

Medlin, W. L., and L. Marsi, Laboratory experiments in fracture propagation, *Soc. Pet. Eng. J.*, 256–268, 1984.

Mindlin, R. D., Waves and vibrations in isotropic elastic planes, in *Structural mechanics*, edited by J. W. Goodier and W. J. Hoff, p. 199, Pergamon, New York, 1960.

Morris, R. L., D. R. Grine, and T. E. Arkfeld, Using compressional and shear acoustic amplitude for the location of fractures, *J. Pet. Technol.*, *16*(6), 623–632, 1964.

Myer, L. R., D. Hopkins, and N. G. W. Cook, Effects of contact area of an interface on acoustic wave transmission characteristics, in *Proceedings of the 26th U.S. Rock Mechanics Symposium*, vol. 1, pp. 565–572, A. A. Balkema, Boston, Mass., 1985.

O'Connell, R. J., and B. Budiansky, Seismic velocities in dry and saturated cracked solids, *J. Geophys. Res.*, *79*, 5412–5426, 1974.

O'Connell, R. J., and B. Budiansky, Viscoelastic properties of fluid-saturated cracked solids, *J. Geophys. Res.*, *82*, 5719–5735, 1977.

Pyrak-Nolte, L. J., Seismic visibility of fractures, Ph.D. dissertation, Dep. of Mater. Sci. and Miner. Eng., Univ. of Calif., Berkeley, 1988.

Pyrak-Nolte, L. J., and N. G. W. Cook, Elastic interface waves along a fracture, *Geophys. Res. Lett.*, *14*(11), 1107–1110, 1987.

Pyrak-Nolte, L. J., L. R. Myer, N. G. W. Cook, and P. A. Witherspoon, Hydraulic and mechanical properties of natural fractures in low permeability rock, in *Proceedings of 6th International Congress of Rock Mechanics, Montreal*, vol. I, pp. 225–232, A. A. Balkema, Boston, Mass., 1987*a*.

Pyrak-Nolte, L. J., L. R. Myer, and N. G. W. Cook, Seismic visibility of fractures, in *Proceedings of the 28th U.S. Symposium on Rock Mechanics, University of Arizona, Tucson*, pp. 47–56, A. A. Balkema, Boston, Mass., 1987*b*.

Raven, K. G., and J. E. Gale, Water flow in natural fractures as a function of stress and sample size, *Int. J. Rock Mech. Min. Sci. Geomech. Abstr.*, *22*, 251, 1985.

Schoenberg, M., Elastic wave behavior across linear slip interfaces, *J. Acoust. Soc. Am.*, *68*(5), 1516–1521, 1980.

Schoenberg, M., Reflection of elastic waves from periodically stratified media with interfacial slip, *Geophys. Prospect.*, *31*, 265–292, 1983.

Spencer, J. W., Stress relaxation at low frequencies in fluid-saturated rocks: Attenuation and modulus dispersion, *J. Geophys. Res.*, *86*, 1803–1812, 1981.

Swan, G., Determination of stiffness and other joint properties from roughness measurements, *Rock Mech. Rock Eng.*, *16*(1), 19–38, 1983.

Walsh, J. B., Seismic wave attenuation in rock due to friction, *J. Geophys. Res.*, *71*, 2591–2599, 1966.

White, J. E., *Underground Sound*, pp. 83–183, Elsevier, New York, 1983.

Winkler, K. W., Frequency dependent ultrasonic properties of high-porosity sandstones, *J. Geophys. Res.*, *88*, 9493–9499, 1983.

Winkler, K. W., Dispersion analysis of velocity and attenuation in Berea sandstone, *J. Geophys. Res.*, *90*, 6793–6800, 1985.

Winkler, K. W., Estimates of velocity dispersion between seismic and ultrasonic frequencies, *Geophysics*, *51*(1), 183–189, 1986.

Winkler, K. W., and A. Nur, Seismic attenuation: Effects of pore fluids and frictional sliding, *Geophysics*, *47*(1), 1–15, 1982.

Yadav, G. D., F. A. L. Dullien, I. Chatzis, and I. F. MacDonald, Microscopic distribution of wetting and non-wetting phases in sandstones during immiscible displacement, *SPE 13213*, Soc. of Pet. Eng., Dallas, Tex., 1984.

Yu, T. R., and W. M. Telford, An ultrasonic system for fracture detection in rock faces, *Can. Min. Met. Bull.*, *66*(729), 96–101, 1973.

N. G. W. Cook and L. R. Myer, Lawrence Berkeley Laboratory, Earth Sciences Division, University of California, 1 Cyclotron Road, Berkeley, CA 94720.

L. J. Pyrak-Nolte, Department of Earth and Atmospheric Sciences, Purdue University, East Lafayette, IN 47907.

(Received January 31, 1989;
revised December 7, 1989;
accepted January 7, 1990.)